Modeling the Yaw Behavior of Tail Fins for Small Wind Turbines

November 22, 2021–May 21, 2024

Mohamed M. Hammam[1] and David Wood[2]

1 Port Said University
2 University of Calgary

NREL Technical Monitor: Brent Summerville

NREL is a national laboratory of the U.S. Department of Energy
Office of Energy Efficiency & Renewable Energy
Operated by the Alliance for Sustainable Energy, LLC

This report is available at no cost from the National Renewable Energy Laboratory (NREL) at www.nrel.gov/publications.

Contract No. DE-AC36-08GO28308

Subcontract Report
NREL/SR-5000-86044
July 2023

Modeling the Yaw Behavior of Tail Fins for Small Wind Turbines

November 22, 2021–May 21, 2024

Mohamed M. Hammam[1] and David Wood[2]

1 Port Said University
2 University of Calgary

NREL Technical Monitor: Brent Summerville

Suggested Citation
Hammam, Mohamed M., and David Wood. 2023. *Modeling the Yaw Behavior of Tail Fins for Small Wind Turbines: November 22, 2021–May 21, 2024*. Golden, CO: National Renewable Energy Laboratory. NREL/SR-5000-86044.
https://www.nrel.gov/docs/fy23osti/86044.pdf.

NREL is a national laboratory of the U.S. Department of Energy
Office of Energy Efficiency & Renewable Energy
Operated by the Alliance for Sustainable Energy, LLC

This report is available at no cost from the National Renewable Energy Laboratory (NREL) at www.nrel.gov/publications.

Contract No. DE-AC36-08GO28308

Subcontract Report
NREL/SR-5000-86044
July 2023

National Renewable Energy Laboratory
15013 Denver West Parkway
Golden, CO 80401
303-275-3000 • www.nrel.gov

NOTICE

This work was authored in part by the National Renewable Energy Laboratory, operated by Alliance for Sustainable Energy, LLC, for the U.S. Department of Energy (DOE) under Contract No. DE-AC36-08GO28308. Funding provided by the U.S. Department of Energy Office of Energy Efficiency and Renewable Energy Wind Energy Technologies Office. The views expressed herein do not necessarily represent the views of the DOE or the U.S. Government.

Cover Photos by Dennis Schroeder: (clockwise, left to right) NREL 51934, NREL 45897, NREL 42160, NREL 45891, NREL 48097, NREL 46526.

Executive Summary

This report describes the aerodynamic modeling of the yaw behavior of tail fins for small wind turbines (SWTs). The analysis is based on unsteady slender body theory (USBT) and is intended to inform a new tail fin module for OpenFAST. Linearized USBT, which has been applied in the past to SWT tail fins, is developed in three main ways. First, it is extended to high yaw angles and aspect ratios by modeling the associated nonlinear vortex dynamics and the chordwise load distribution, respectively. Second, we consider the effect of time-varying wind speed. The extended theory is compared to recent unpublished measurements at the University of Perugia, Italy, for the yaw behavior of delta, elliptical, and rectangular tail fins without a rotor and nacelle. The fins were released from initial yaw angles of -40° and -80°; the latter is of sufficient magnitude to show the importance of the nonlinear yaw dynamics. Further, the friction in the model tail fin bearings was measured and modeled. Some coefficients of the extended moment equations were determined from previous computational simulations and experiments. The report provides equations for many of the coefficients describing geometric features that modify a delta planform. These include sweep angle, taper ratio, and notch ratio as well as the aspect ratio. Significant improvement in accuracy was achieved by using system identification techniques to optimize some of the model constants that are the least certain. We conclude that extended USBT is accurate for all generic tail fin shapes that we considered and is, therefore, very suitable for inclusion in aeroelastic codes for SWTs. The final development is of a general nonlinear equation for yaw response that is simpler than the extended USBT and is also suitable for inclusion in OpenFAST. The two nonlinear models are used to highlight the geometric requirements for good tail fin design.

Acknowledgments

The model development described in this report would have been impossible without the concurrent experimental study by Francesco Castellani and his group at the University of Perugia. The authors are also grateful to our colleagues at the National Renewable Energy Laboratory, primarily Emmanuel Branlard, Jason Jonkman, Abhineet Gupta, and Brent Summerville, for their many comments and suggestions.

Table of Contents

List of Figures

List of Tables

1 Introduction

Small wind turbines (SWTs) with a power output less than about 20 kW often use a tail fin to align the rotor with the wind, whereas all large turbines have a motorized yaw drive. The "passive" system on SWTs is much cheaper but comes with a price: it may not be easy to limit the yaw rate about the tower, which can lead to high gyroscopic loads. Further, tail fins are intrinsically unable to completely track wind direction changes, which can lead to reduced power output. Despite the importance of a well-designed tail fin for efficient and safe SWT operation, the aeroelastic modeling of tail fins is not well developed. For example, the well-known aeroelastic software OpenFAST v3.4 [1] has just been augmented by the tail fin module from FAST v7, which was released in 2002. The module uses a simple lookup table of tail fin lift and drag to determine the forces and moments. A major aim of this work is to provide the theoretical background for a new tail fin module for OpenFAST.

There are several rules-of-thumb for tail fin design, but very little data on their behavior, (Bradney, Evans, and Clausen 2018). The yaw response of generic tail fin shapes in the absence of a rotor was measured in a wind tunnel by (Singh, Hemmati, and Wood 2012) for a single wind speed and low release angle. By characterizing the response in terms of the damping ratio and natural frequency, they found that a delta wing is a representative shape for tail fins. Since a delta wing is also the generic shape used to develop unsteady slender body theory (USBT), which is the basis for the analysis in this report, we will take the delta to be the baseline shape for tail fins. The other generic shapes we consider are ellipses and rectangles. Apart from being simple shapes, they share the importance of flow separation from the edges in determining the aerodynamic forces and moments. This makes it is reasonable to ignore Reynolds number effects in modeling them.

A tail fin is most needed for turbine starting. When subjected to a wind gust, an initially stationary rotor may have its axis at a large yaw angle, γ, to the wind, (Wood 2011). One scenario for large γ is the following: If the turbine center of mass is not aligned with the tower axis and the tower is not exactly vertical, then the stationary turbine will have a preferred orientation, which can be at any γ. Tail fins also help to reduce γ during power production, which is important because a yaw error reduces the output power by a factor between $\cos^2\gamma$ and $\cos^3\gamma$, (Wood 2011). Yaw alignment also relates to the gyroscopic bending moments on the blades and main shaft. Their magnitude depends on the product of blade inertia, blade angular velocity, and yaw rate relative to a fixed observer. They can be the major ultimate loads on an SWT, (Wood 2011), and can also contribute significantly to the fatigue loads. (Evans et al. 2021).

The linearized analysis of tail fin dynamics based on USBT (Wood 2011; Singh, Hemmati, and Wood 2012; Bradney, Evans, and Clausen 2018) assumes that γ is small and the angle of attack of the tail fin, α, is the same as γ. Then the yaw moment of the tail fin is due entirely to the lift force acting somewhere on the tail fin chord. We extend USBT to high γ by including the nonlinear dependence on γ and separating the representation of α from that of γ. This leads to both lift and drag causing yaw moments on the tail fin. A general expression for the yaw moment when wind direction varies is then developed.

The next section describes the basic USBT for low-aspect-ratio delta wings. The theory is extended to high angles for steady and unsteady flow in Section 2.1.1 and to high aspect ratios in Section 4. The short Section 5 gives the general force and moment equations for a tail fin of any planform prior to considering elliptic fins in Section 6 and rectangular ones in Section 7. The following section compares the models to wind tunnel experiments on tail fin response in the absence of a rotor and nacelle for all three planforms. Section 9 analyzes the effect of yaw bearing friction, which is important at low wind speed, U. All the parameters used in the USBT model to this point were determined from prior analytic, computational, and experimental studies. Section 10 describes the use of system identification techniques to show that (usually) small changes to these parameters can significantly improve the accuracy of the modeled response and can help to identify the most important components of the model. Section 11 describes the extension of the model to more complex versions of the delta planform. Different planforms are assessed in Section 12 partly in terms of their response at very high angles where the flow direction is reversed. The desirable features of planforms to give good low and high angle behavior are noted. Section 13 describes a reduced form of the nonlinear moment equation, which is also suitable for OpenFAST. This model is assessed for the case where the maximum tail fin chord, c_0, is comparable to the tail boom length, x_p, and a reduced model is derived assuming $c_0 \ll x_p$ for application to a wide range of planforms using system identification. Section 14 compares the present yaw response model to the polar model in v3.4 of OpenFAST. The final section contains a summary of the

[1] https://www.nrel.gov/wind/nwtc/fast.html

report, recommendations for including the full and reduced models in OpenFAST, and the conclusions. The appendix documents one of the MATLAB systems identification codes used in Section 10. This is intended to be a guide for the future analysis of wind tunnel tests to determine the model parameters to be used in OpenFAST.

2 Mathematical Model

2.1 Potential Flow Modeling

We start by considering the potential flow over a delta tail fin with aspect ratio (AR) less than one. For a wing of any geometry, $AR = b_0^2/S$ where b_0 is the span, and S the planform area. The restriction to slender, low-AR delta wings allows the application of USBT, which is relatively simple. An extension of the model to high-AR tail fins is described in Section 4. In contrast to existing tail fin analyses, we separate the angle of attack, α from the yaw angle, γ. The resultant force acting on the tail fin then has both lift and drag components which contribute to the yaw moment around the yaw axis. The analysis is limited to vertical tail fins with no camber.

The non-inertial coordinate system is fixed to the tail fin; x is aligned with the chord of the tail fin, and the motion of the tail fin is in the inertial (x_i, y_i) plane. The vertical z-direction is parallel to the yaw axis, as shown in Figure 1. The wind velocity, $U(t)$, makes an angle γ_w with the inertial x_i direction and is a function of time. The coordinate system of the vertical fin rotates around the z-axis with the angle $\gamma + \gamma_w$ relative to the inertial coordinates (x_i, y_i, z). Angles γ and γ_w are shown in Figure 1. This coordinate system simplifies the consideration of the angular velocity of the tail fin, $\Omega(t)$, where $\Omega(t) = \dot{\gamma} + \dot{\gamma}_w$, and the dots denote time derivatives. For later use, we define a characteristic moment arm r, which is approximately x_p, the tail boom length from the tower axis to the apex of the delta wing, in this case, or the start of the tail fin in general. The origin N lies on the top of the tower axis for both coordinate systems. The structural velocity of the tail fin at the apex is V_{el}. This velocity includes the contribution from the rotational speed and additional translational velocities caused by the tower motion.

In addition, the energy lost to the rotor will cause an induced velocity on the tail fin, V_{in}, whose determination is *not* considered here. The velocity polygon of these and the resultant velocity V is shown in Figure 1 along with its angle of attack, α. Figure 2a shows a straight-edged delta tail fin with chord c_0 and span b_0, and $AR = 2b_0/c_0$. The tail fin moment of inertia combined with that of the tail boom around the z-axis is I_a at the tail fin apex. Finally, it is assumed that the tail boom does not experience any aerodynamic force or moment.

The analysis is based on USBT as described in detail in (Katz and Weihs 1979) and Section 13.9 of (Katz and Plotkin 2001); only a brief introduction is given here. Slenderness implies that the cross flow (in the (y,z) plane) is dominant and locally two-dimensional. Since a slender tail fin has $c_0 \gg b_0$, then $x \gg y, z$ in general, and

$$\frac{\partial}{\partial x} \ll \frac{\partial}{\partial y}, \frac{\partial}{\partial z} \tag{2.1}$$

Ignoring the streamwise flow in the continuity equation leads to

$$\nabla^2 \phi \approx \frac{\partial^2 \phi}{\partial y^2} + \frac{\partial^2 \phi}{\partial z^2} = 0 \tag{2.2}$$

for the velocity potential ϕ. Eqn. (2.2) is subject to the velocity boundary conditions for an impermeable surface transformed to the non-inertial coordinates as

$$(\nabla \phi + V).n = 0 \tag{2.3}$$

where n is the unit vector normal to the tail fin surface, with coordinates $n = [0, -1, 0]$ in the tail fin system (we note that the choice of direction along the y-axis does not change this definition). The resultant velocity, V, as shown in Figure 1, is given by

$$V = U - V_{el} + V_{in} \tag{2.4}$$

Defining the resultant velocity components, $[V_x, V_y, V_z]$, in the tail fin coordinate system (x, y, z) as

$$V_x = U_x - V_{x,el} + V_{x,in}, \tag{2.5}$$

$$V_y = U_y - V_{y,el} + V_{y,in}, \quad \text{and} \tag{2.6}$$

$$V_z = U_z - V_{z,el} + V_{z,in} \tag{2.7}$$

where $U = [U_x, U_y, U_z]$ in the (x, y, z) coordinates is shown in Figure 1. Ω is the angular velocity of the tail fin with respect to the inertial frame of reference (x_i, y_i, z); $\Omega = [\Omega_x, \Omega_y, \Omega_z]$. $V_{el} = [V_{x,el}, V_{y,el}, V_{z,el}]$ is the structural velocity of the tail fin apex, and $V_{in} = [V_{x,in}, V_{y,in}, V_{z,in}]$ is the induced velocity from the turbine wake, both defined in the (x, y, z)

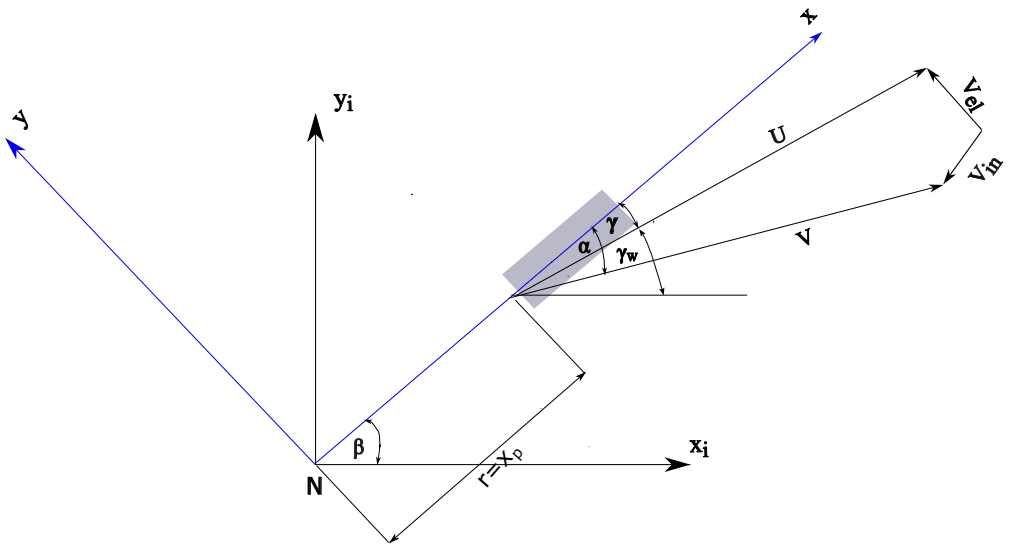

Figure 1. Schematic plan view of tail fin motion and coordinate systems. The tail fin of exaggerated thickness is shaded.

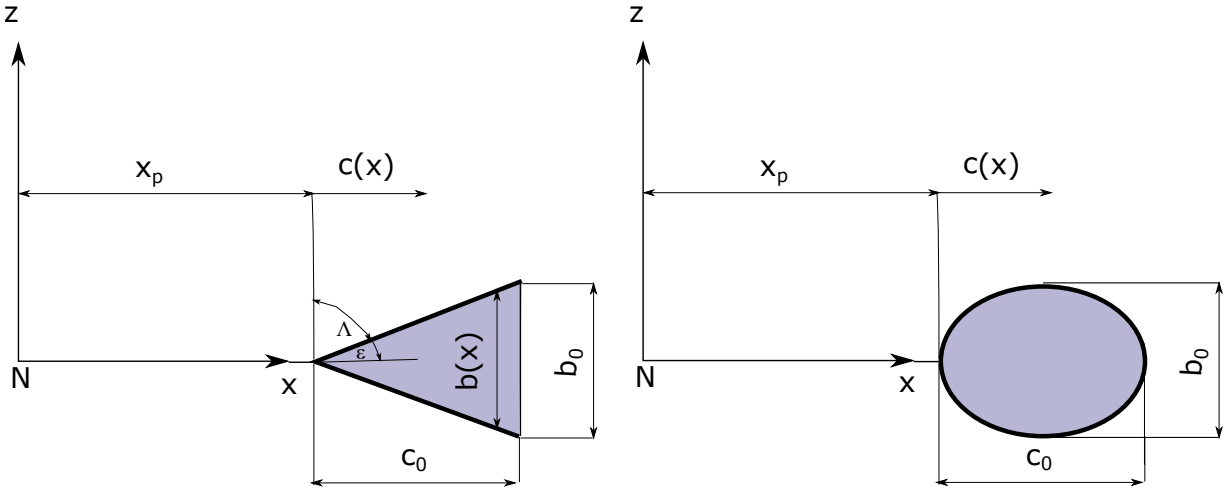

(a) Delta tail fin. **(b) Elliptic tail fin.**

Figure 2. Geometry of generic tail fin planforms.

coordinates. In the absence of tower motion $V_{el} = \Omega \times r$,where $\Omega = \dot{\beta}$, $\beta = \gamma + \gamma_w$, and $r = [x_p, 0, 0]$. Substituting these relations in Eqn. (2.3) results in

$$\left[\frac{\partial \phi}{\partial x} + V_x, \frac{\partial \phi}{\partial y} + V_y, \frac{\partial \phi}{\partial z} + V_z\right] \cdot [0, -1, 0] = 0 \tag{2.8}$$

The equation reduces to

$$\frac{\partial \phi}{\partial y} = -V_y \equiv W(x,\, t) \tag{2.9}$$

where $W(x,t)$ is the spanwise induced downwash, which is independent of z. The pressure difference, Δp, is determined from (Katz and Plotkin 2001; Katz and Weihs 1979) as

$$\Delta p = 2\rho \left[\frac{\partial \Delta \phi}{\partial t} + V_x \frac{\partial \Delta \phi}{\partial x}\right] \tag{2.10}$$

The reduced form of Eqn. (2.2) results in a lifting line problem with the circulation distribution at any x having an elliptic form as function of z, (Katz and Plotkin 2001):

$$\Gamma(z) = -W(x,t)\ b(x)\ \sqrt{1-\left[\frac{2z}{b(x)}\right]^2} \tag{2.11}$$

ϕ can be written in terms of the circulation distribution in Eqn. (2.11) as Eqn. (13.88) in (Katz and Plotkin 2001):

$$\phi(x,\pm 0,z,\ t) = \pm\Gamma(z)/2 = \mp\frac{W(x,t)\ b(x)}{2}\sin\theta \tag{2.12}$$

Note that negative W leads to positive circulation on the top surface of the tail fin and the reverse on the bottom surface. $\cos\theta = 2z/b(x)$ is the spanwise coordinate of the tail fin, where $b(x)$ is shown in Figure 2 for two of the generic planforms. The contribution to the normal force, N, acting on the tail fin at any x is given by

$$\frac{dN}{dx} = \int_{-b(x)/2}^{b(x)/2} \Delta p dz \tag{2.13}$$

and substituting Eqn. (2.12) into Eqn. (2.10), leads to

$$\frac{dN}{dx} = -\rho\left[\frac{\partial W(x,t)\ b(x)}{\partial t} + V_x\frac{\partial W(x,t)\ b(x)}{\partial x}\right]\int_{-b(x)/2}^{b(x)/2}\sqrt{1-\left[\frac{2z}{b(x)}\right]^2}\,dz \tag{2.14}$$

The integral in Eqn. (2.14) is easily evaluated to give

$$\frac{dN}{dx} = -\frac{\pi\rho}{4}\left[b^2(x)\frac{\partial W(x,t)}{\partial t} + V_x\frac{\partial W(x,t)b^2(x)}{\partial x}\right] \approx -\frac{\pi\rho}{4}\left[b^2(x)\frac{\partial W(t)}{\partial t} + V_x W(t)\frac{db^2(x)}{dx}\right] \tag{2.15}$$

where the approximate equation can be used if W does not vary significantly over the tail. This is likely to be the case when $c_0/x_p \ll 1$. The appearance of $b(x)$ shows the influence of tail fin planform. In the proposed OpenFAST module, the tail fin apex ($x = x_p$) will be the reference point, so we determine M_a, the yaw moment due to $N(x)$ around the apex as

$$M_a = \int_{x_p}^{x_p+c_0}\frac{dN}{dx}\ (x-x_p)\ dx \tag{2.16}$$

where $b(x) = b_0(x-x_p)/c_0 = (x-x_p)AR/2$ for $x \geq x_p$ for a straight-edged delta wing. Using this in the full form of Eqn. (2.15) and substituting into Eqn. (2.16), gives the moment as

$$M_a = -\frac{\pi\rho}{16}AR^2\int_{x_p}^{x_p+c_0}\left[(x-x_p)\frac{\partial W(x,t)}{\partial t} + (x-x_p)V_x\frac{\partial W(x,t)}{\partial x} + 2V_x W(x,t)\right]\ (x-x_p)^2\ dx \tag{2.17}$$

Performing the integrals in Eqns. (2.15) and (2.17) by assuming W is constant with x for $x_p \gg c_0$ gives

$$N = -0.5\rho A_{tf}K_p\left[\frac{c_0}{3}\frac{\partial W}{\partial t} + V_x W\right] \tag{2.18}$$

and

$$M_a = -0.5\rho A_{tf}K_p\left[\frac{c_0^2}{4}\frac{\partial W}{\partial t} + \frac{2c_0}{3}V_x W\right] \tag{2.19}$$

were $K_p = \pi AR/2$ is the potential flow coefficient and $A_{tf} = b_0c_0/2$ is the area of the delta tail fin. Note that the first term in the square brackets for force and moment is the unsteady term and would be zero for steady yaw. The second terms express the steady state force and moments. It follows that the center of pressure on a delta tail fin is at $2c_0/3$ from x_p. If only aerodynamic forces act on the tail fin, the equation of its unsteady motion around the tail fin apex is simply

$$I_a\ddot{\beta} = M_a \tag{2.20}$$

where I_a is the tail fin moment of inertia around the apex, and the analysis can be extended to any planform.

2.1.1 Vortex Flow Modeling

Steady State Modeling

The mathematical model developed in the previous section assumes potential flow. Sharp, thin leading-edges, however, generate vortices which, in turn, cause extra forces on the fin and make its motion nonlinear. The first contribution of this analysis is the extension of the potential model to include vortex effects based on the theory of (Polhamus 1966). For a stationary delta tail fin without a rotor, the normal force is determined from integrating Eqn. (2.15) over x to give

$$N = \frac{\pi}{4}\rho\, b_0^2\, U^2 \cos\gamma\, \sin\gamma, \tag{2.21}$$

and the potential normal force coefficient is

$$C_{N,p} = \frac{4N}{\rho U^2 b_0 c_0} = \frac{\pi AR}{2}\cos\gamma\,\sin\gamma \tag{2.22}$$

The angle of attack α is related to γ through the sine rule of the velocity polygon shown in Figure 1. Using the trigonometric identities in (Kershner 1971):

$$\tan\alpha = -V_y/V_x \tag{2.23}$$

For a stationary tail fin without a rotor, $\alpha = \gamma$, and Eqn. (2.22) recovers the potential nonlinear normal force coefficient of a steady, stationary delta wing, (Polhamus 1966). His delta wing theory uses the leading-edge suction analogy to modify the steady normal force coefficient in Eqn. (2.22) to have two components:

$$C_N = C_{N,p} + C_{N,v} \tag{2.24}$$

where the potential normal force coefficient is

$$C_{N,p} = K_p\,\cos\gamma\,\sin\gamma \tag{2.25}$$

The vortex component is

$$C_{N,v} = \frac{K_v}{K_p} C_{N,p} |\tan\gamma| = K_v\,|\sin\gamma|\sin\gamma \tag{2.26}$$

The potential flow coefficient, K_p, depends only on the planform as given by Eqn. (2.22). The vortex lift coefficient, K_v, is bounded by $3.14 \le K_v \le 3.45$ for $0 \le AR \le 4$ for a straight-edged delta wing, (Polhamus 1966). K_v can be determined from the "suction force" perpendicular to the leading-edge as in the thin airfoil analysis of (Brown 1946). It is assumed that the pressure distribution in the neighborhood of the leading-edge, where the vortex forms, is identical with that for a two-dimensional flat plate. The suction force, F_s, normal to the edge of the plate per unit length of edge is given by

$$\frac{dF_s}{dR} = 2\rho\pi G^2 \tag{2.27}$$

where R is measured along the leading-edge and G is a factor which is found by requiring the suction force to generate a thrust component that cancels the drag of a flat plate. K_v is considered further in Section 11.1.

Total Leading-Edge Vortex Force

Vortex flow over the tail fin causes a considerable load that affects the damping of the motion. For a yawing tail fin, the total normal force acting on the tail fin from the vortex flow is

$$F_s = \rho K_v \frac{AR}{4}\int_{x_p}^{x_p+c_0} W^2(x-x_p)dx = \rho K_v \frac{AR}{4}\int_{x_p}^{x_p+c_0} {V_y}^2(x-x_p)dx \tag{2.28}$$

When $W = -V_y$ is constant with x, the vortex force is simply

$$F_s = 0.5\rho A_{tf} K_v W^2 \tag{2.29}$$

while the yaw moment at the apex is given by

$$M_a = \frac{2c_0}{3} 0.5\rho A_{tf} K_v W^2 = \frac{2c_0}{3} F_s \tag{2.30}$$

and it is important that the sign of the different terms in W are preserved. The leading-edge vortex (LEV) does not contribute to $\partial\phi/\partial t$, (Amiet 1995; Wu 1961), so its unsteady effect comes from the change in strength and location as α changes, (LeMay, Batill, and Nelson 1990; Lan 1982). This issue will be dealt with in Section 2.1.1.

Separation at High Angle of Attack

At very high α, depending on AR, full flow separation occurs over the tail fin as it does over a normal flat plate where the normal force is determined completely by the drag coefficient C_{Dc}. The normal force coefficient for separated flow, $C_{N,s}$, can be approximated as

$$C_{N,s} = C_{Dc} \sin\gamma \tag{2.31}$$

C_{Dc} for any flat planform is that for a normal flat plate which can be approximated as (Larson 2012)

$$C_{Dc} = C_{2D}\left[1 - \frac{5R_a}{1 - 3.2\sqrt{R_a} + 15.15R_a - 0.75R_a^2}\right] \tag{2.32}$$

where $C_{2D} = 2$ is the drag coefficient of a flat plate when it is normal to the flow, and $R_a = b_0/c_0 = AR/2$. From Eqn. (2.32), $C_{Dc} = 1.18$ for $AR = 2$. This value is lies between 1.1 and 1.4 for delta wings of different AR in (Jarrah 1989). So, a value of $C_{Dc} = 1.3$ should be reasonable for most tail fins. This value is used throughout the analysis.

Vortex Breakdown

In following the wind, the tail fin α changes almost at the same rate as the yaw rate as can be seen from Eqn. (2.23). In these dynamic conditions, LEVs will burst at a certain angle, (Jouannet and Krus 2002). When the vortex detaches from the wing at the apex, the fully separated flow is modeled as in Section 2.1.1. The normal forces can be scaled to give the contribution of the three force components: the potential flow, vortex flow and break down, vortex burst, and full separation. The total normal force is then the sum of the potential and vortex force components, with the vortex force dependent on the location of vortex bursting. The normal force for a stationary tail fin can be modeled as

$$C_N = x_1 K_p \cos\gamma \sin\gamma + x_2 K_v |\sin\gamma| \sin\gamma + (1 - x_3) C_{Dc} \sin\gamma \tag{2.33}$$

where x_1, x_2, and x_3 are the "separation functions" for the contribution of each force component on a tail fin pitching at the rate of $\dot{\gamma}$ at the corresponding α. All three functions can be modeled by a first-order differential equation, (Goman and Khrabrov 1994):

$$\tau_1 \frac{\partial x_i}{\partial t} + x_i = x_{i,0}(\alpha - \tau_2 \dot{\alpha}) \tag{2.34}$$

where $\tau_1 \simeq 8c_0/U, \tau_2 \simeq 0.5c_0/U$ are time constants, and $i = \{1,2,3\}$. $\dot{\alpha} \simeq \dot{\gamma}$ is the pitch rate, and $x_0(\alpha - \tau_2\dot{\alpha})$ is a forcing function that decays exponentially as in (Fan and Lutze 1996):

$$x_{i,0}(\alpha - \tau_2 \dot{\alpha}) = (1 + \exp[\sigma(\alpha - \tau_2\dot{\alpha} - \alpha_i^*)])^{-1} \tag{2.35}$$

where σ is an empirical constant that expresses the rate of decay of the forcing function. The characteristic time c_0/U is very small for a tail fin so the term $\tau_2\dot{\alpha}$ can be neglected. Thus

$$x_{i,0}(\alpha - \tau_2 \dot{\alpha}) = \left(1 + \exp[\sigma(\alpha - \alpha_i^*)]\right)^{-1} \tag{2.36}$$

where α_i^* can have different values for each flow component. For potential flow, it is the stall angle of the tail fin, and for vortex flow, the angle of attack at which the vortex from the tail fin apex bursts. At this angle, the separation function $x_i = 0.5$, as can be seen from Eqns. (2.34) and (2.35). The resulting force and moments equations for the case $x_p \gg c_0$ of potential flow equations, (2.18) and (2.19), are modified to include the effect of vortex flow from Eqns. (2.29) and (2.30), and the separation functions as

$$N = -0.5\rho A_{tf} K_p \left[\frac{c_0}{3}\frac{\partial W}{\partial t} + x_1 V_x W\right] - 0.5\rho A_{tf}\left[x_2 K_v + (1 - x_3) C_{Dc}\right] W^2 \tag{2.37}$$

and

$$M_a = -0.5\rho A_{tf} K_p \left[\frac{c_0^2}{4}\frac{\partial W}{\partial t} + \frac{2c_0}{3} x_1 V_x W\right] - \frac{2c_0}{3} 0.5\rho A_{tf}\left[x_2 K_v + (1 - x_3) C_{Dc}\right] W^2 \tag{2.38}$$

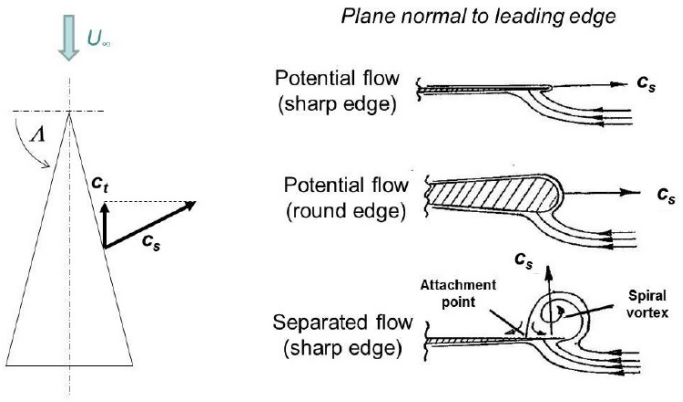

Figure 3. Suction analogy concept. C_s, suction force coefficient and its thrust coefficient component, C_t, (Luckring 2016).

,

2.1.2 Tangential Force Component

The tangential force, T, in the x-direction, acting on an uncambered tail fin cannot contribute to the yaw moment. T, however, can contribute to the structural loads on the yaw assembly and tower and so is needed for a complete dynamic analysis. The LEV force cancels the chordwise force resulting from the potential flow, (Pedersen and Żbikowski 2006). Unsteady forces resulting from the potential flow can be estimated by replacing $\partial W/\partial t$ in Eqn. (2.15) by $-\dot{\beta}W$, (Pedersen and Żbikowski 2006):

$$\frac{dT}{dx} = \frac{\pi\rho}{4} b^2(x)\dot{\beta}W \tag{2.39}$$

so the total tangential force for a constant W with x is

$$T = \frac{c_0}{3} 0.5\rho A_{tf} K_p \dot{\beta} W \tag{2.40}$$

In fully separated steady flow over a sharp leading-edge, there is no tangential force acting on the surface, as can be seen in Figure 3, (Luckring 2016). Cross sections normal to the leading-edge are shown on the right for three flows. The top and middle parts show the suction force generated due to leading-edge singularity for attached flow at the leading-edge of sharp and round edge wings. The bottom part shows full separation over a highly swept sharp delta wing where the LEV forms, separates, and reattaches to the surface, generating a normal force equal to the suction force in the top figure of normal attached flow. This makes the normal force the resultant force acting on delta wings.

3 Synthesizing the Normal Force Coefficient for Delta Tail Fins

C_N can be determined from Eqn. (2.33) up to $\alpha = 90°$. The model contains the separating functions x_1, x_2, and x_3 that appear in Eqn. (2.36). This model, however, contains unknown coefficients that depend on the AR. In this section these coefficients are estimated from experimental data up to high α. In some of the references used in this section, the delta wings are identified by the sweep angle, Λ, defined in Figure 2a, and related to AR by $AR = 4/\tan(\Lambda)$.

The procedure followed to calibrate the different parameters in the model is taken from (Jouannet and Krus 2007). τ_1 expresses the strength of the LEV as α changes. It was found from the unsteady LEV model in (Dore 1966) that the strength reaches its steady value in time $\tau_1 = c_0/U$, which is typically small for tail fins. Assuming that the full strength develops instantaneously makes the separation function for a tail fin equal to its forcing function given by Eqn. (2.36).

The functions x_1, x_2, and x_3 express the relative importance of potential flow, vortex flow, and cross flow, respectively. (Jouannet and Krus 2007) recommended that α_1^* be the angle at which the vortex breaks down at the trailing edge and $\alpha_2^* = \alpha_3^*$ be the α at which the vortex breaks down at the wing apex. (Jouannet and Krus 2007) give the transition constants σ to be between 0.2 and 0.4. It was found, however, that $\sigma_1 = 0.3$ and $\sigma_2 = 0.1$ are good choices for most delta wings with $\sigma_3 \leq \sigma_2$. To get α_1^* and α_2^*, Figure 4 from (Lowson and Riley 1995) could be used. Setting α_1^* to be the stall angle at each Λ, however, was found to give better results. A simple procedure is that $\alpha_1^* = 35°$ for $\Lambda = 70°$ and changes by half the change in Λ. To validate the model, (Jarrah 1989) measured C_N for delta wings of $AR = 1, 1.5$, and 2. As recommended above: $\sigma_1 = 0.3, \sigma_2 = 0.1$, and $\sigma_3 = 0.05$ were chosen for all cases. α_1^* was chosen to be the stall angle and $C_{Dc} = 1.3$. α_2^* was chosen to be the angle of attack of breakdown at the apex, as found from Figure 4 for the corresponding Λ.

For $AR = 1$, $\alpha_1^* = 38°$ and $\alpha_2^* = 55°$ for $\tan\Lambda = 4$. $\alpha_3^* = \alpha_2^* + 5 = 60°$. Comparison between measurements and the model for $AR = 1$ is shown in Figure 5(a). For $AR = 1.5$, $\alpha_1^* = 40°$ and $\alpha_2^* = 48°$ for $\tan\Lambda = 2.7$. $\alpha_3^* = \alpha_2^* + 5 = 53°$. The stall angle is found to be higher than the recommended value for $\Lambda = 70°$ of $\alpha_1^* = 35°$. Theory and measurements for $AR = 1.5$ are shown in Figure 5(b). For $AR = 2$, $\alpha_1^* = 40°$ and $\alpha_2^* = 40°$. $\alpha_3^* = \alpha_2^* + 5 = 45°$. The stall angle is higher than that recommended for $\Lambda = 63°$ of $\alpha_1^* = 32.5°$. Measurements and the model for $AR = 2$ are compared in Figure 6(a). For this case the stall is deeper than at lower AR. So, a value of $\sigma_3 = \sigma_2 = 0.1$ was chosen instead of the default of $\sigma_3 = 0.05$, and the results for this case are shown in Figure 6(b).

These results show the stall angle does not change much with AR, and $\alpha_1^* = 39°$ should be representative of delta tail fins. The angle of vortex breakdown at the apex α_2, however, decreases by about 20° for an increase of 1 in AR and approaches the stall angle as AR increases. This leads to sharper stall of delta wing at higher AR and an increase in the value of the transition parameter σ_3 of flow separation for high AR.

The above conclusions are preliminary only but sufficient for comparing the theoretical model to the wind tunnel tests in Section 8. A more systematic identification of the parameters will be done in Section 10.

3.1 Aerodynamic Coefficients of Tail Fins in Reverse Flow

For the reasons given in the Introduction, a tail fin can experience reverse flow, particularly during the starting of a SWT. Extending the aerodynamic model to cover α over the range of $\pm 180°$ is likely to be important for accurate prediction of the yaw response for operating turbines.

Experiments on reverse delta wings (RDW) show lower maximum lift and drag with stall at higher α compared to a "normal" delta wing (DW), (Lee and Ko 2016; Mahgoub and Cortelezzi 2020; Gibson and Gerhardt 1993). This behavior is also considered in the NREL Aerodyn code for modeling the flow over wind turbine blades in reverse flow, (Jonkman et al. 2015). They reflect and scale the lift coefficient by a factor of 0.7, but the drag coefficient is not changed. The stalling mechanism for RDWs is different from a normal DWs vortex breakdown, (Lee and Ko 2016).

This reduction in aerodynamic forces for an RDW should be taken into account when choosing a suitable planform as it could reduce the turbine yaw response and increase its starting time. There is no reduction for tail fins with planforms symmetric in x, such as rectangular, elliptical, and diamond shapes. These planforms, however, may give poorer response in normal flow characterized by small distance to the center of pressure and shorter moment arm length.

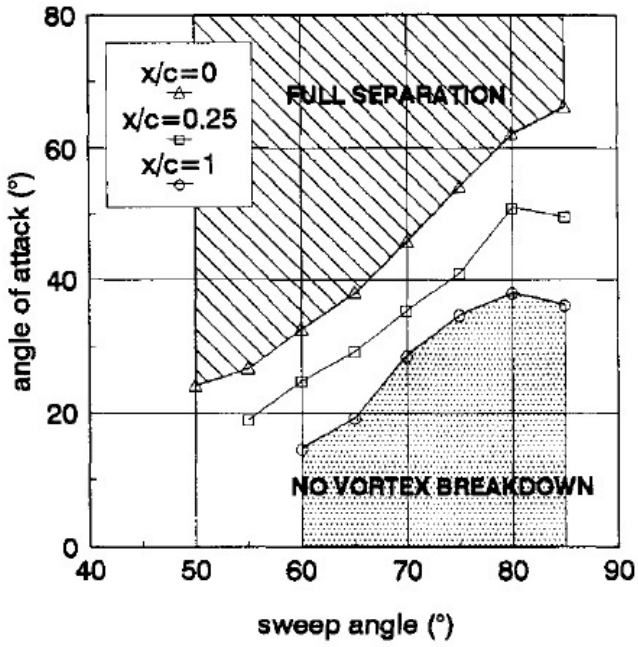

Figure 4. Flow regimes over a delta wing, (Lowson and Riley 1995).The figure is used to determine the angle of attack at which the vortex detaches at the apex (x/c=0), which is equal to $\alpha_2^* \approx \alpha_3^*$.

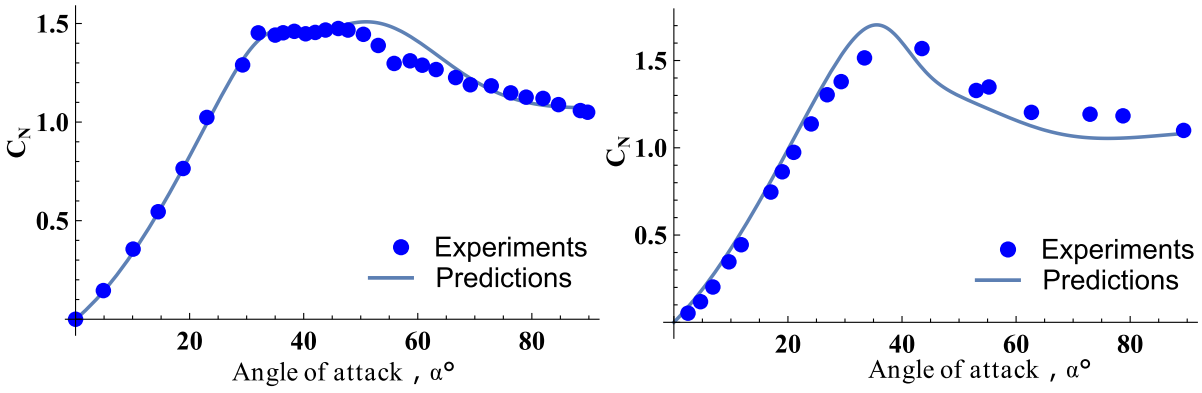

(a) $AR = 1.0$ **(b)** $AR = 1.5$.

Figure 5. Predicted normal force (solid line) compared to the experimental data of (Jarrah 1989) (blue dots) for delta wings.

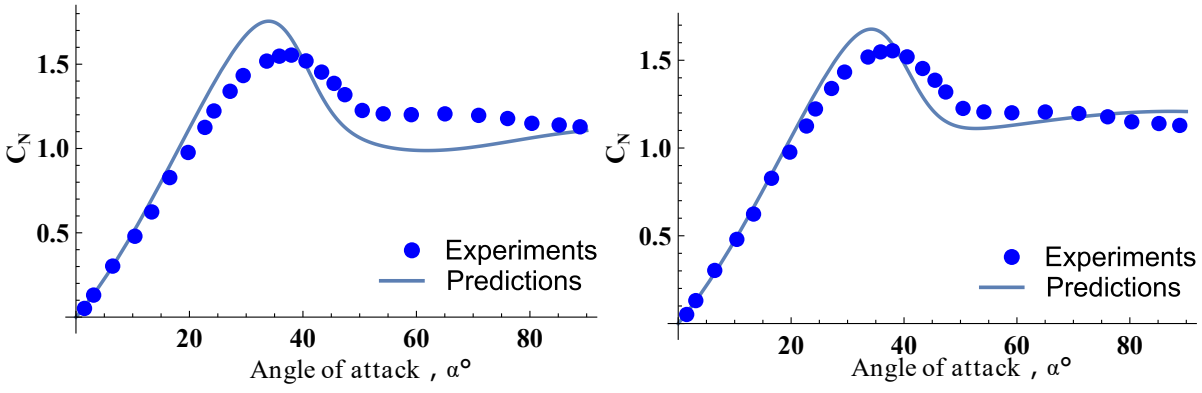

(a) $\sigma_3 = 0.05$ **(b)** $\sigma_3 = 0.1$

Figure 6. Predicted normal force (solid line) compared to the experimental data of (Jarrah 1989) (blue dots) for a delta wing of $AR = 2$.

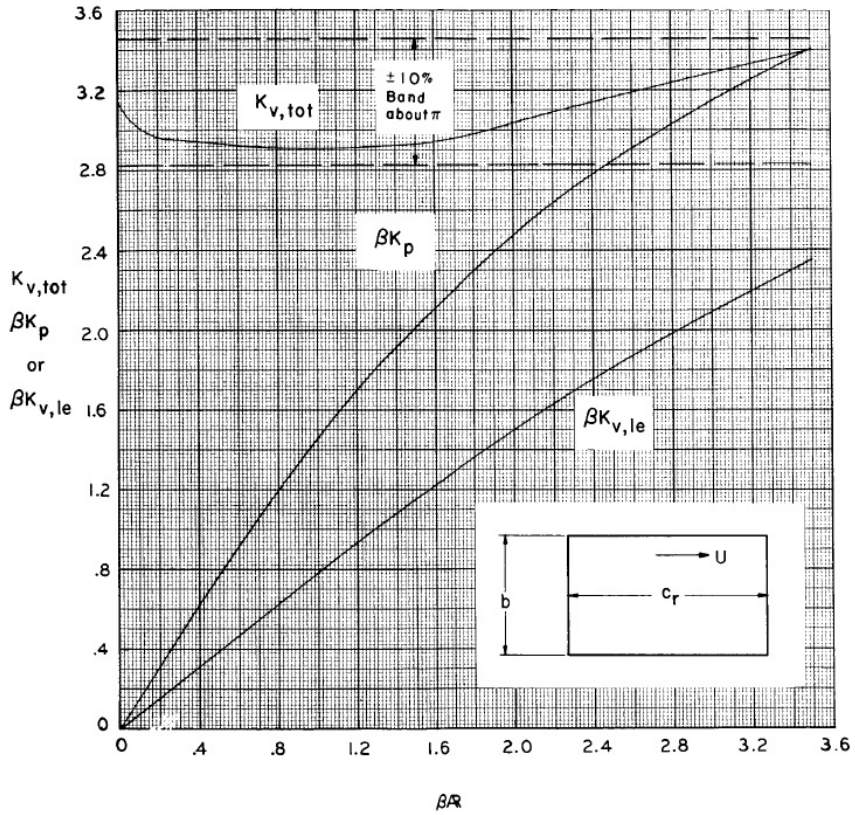

Figure 7. Variation of K_p, $K_{v,le}$, and $K_{v,tot}$ with aspect ratio for rectangular wings, (Lamar 1974). $\beta = \sqrt{1-M^2} = 1$, where M is the Mach number taken here to be zero.

For an RDW, the loss of lift is most likely due to the small strength of the LEV. It can be modeled as a rectangular tail fin with a LEV generated over its base without the side edge vortices that exist on a rectangular plate. It can be seen from (Lamar 1974) that LEV coefficient $K_{v,le}$ for a rectangular plate is much less than the side edge coefficient K_{vse}. This is shown in Figure 7 where the total coefficient $K_{v,tot} = K_{v,le} + K_{v,se}$.

To model the aerodynamic coefficients for an RDW, we take the potential flow coefficient K_p to be the same as for a DW, as argued by (Lee and Ko 2017). K_v, however, is reduced. $K_{v,le}$ for a rectangular tail fin AR is determined from Figure 7 by setting the Mach number, M to zero. Also, the transition angles α^* are higher for an RDW compared to a DW. Both these effects will scale down and shift the lift coefficient to higher α. This stall delay is governed by choosing α_1^* for an RDW to be higher than for a DW. This model is used to predict the lift coefficient of a DW and an RDW of $\Lambda = 65^\circ$ from (Lee and Ko 2017) for which $K_p = 2.1$ for both DW and RDW. In contrast, the DW $K_v = \pi$ whereas $K_v = 1.4$ for an RDW from Figure 7 for $AR = 1.86$. For a DW: $\alpha_1^* = 35^\circ$, $\alpha_2^* = 38^\circ$, and $\alpha_3^* = 45^\circ$. $\sigma_1 = 0.3$, and $\sigma_2 = \sigma_3 = 0.1$ to capture the deep stall. For an RDW: $\alpha_1^* = \alpha_2^* = 40^\circ$, and σ_1, σ_2 and σ_3 were chosen to be the same as for a DW. It should be noted that α_2^* for a DW is chosen from Figure 4 for the corresponding Λ and $\alpha_3^* = \alpha_2^* + 5^\circ$. The predictions using these settings are shown in Figure 8(a).

Figure 8 shows a change in slope of the potential lift between the DW and RDW. This decrease in slope could be modeled by reducing the value of σ_1 or increasing the rate of decay of the potential lift with α. The behavior of the aerodynamic coefficient model as σ changes is shown in Figure 9. These changes in slope could be reproduced by decreasing σ_1 to allow the potential lift to develop slowly. $\sigma_1 = 0.1$ was chosen for the DW and $\sigma_1 = 0.03$ for the RDW. The values of $\sigma_2 = \sigma_3 = 0.1$ were kept the same. The predictions for this case are shown in Figure 8(b). A significant improvement is achieved by changing the values of the potential flow transition constant σ_1 to capture the change in lift coefficient slope, as seen in Figure 8(b). This demonstrates sensitivity of the lift coefficient to the model parameters, which will change the yaw response. This issue is addressed in conjunction with the system identification study in Section 10.

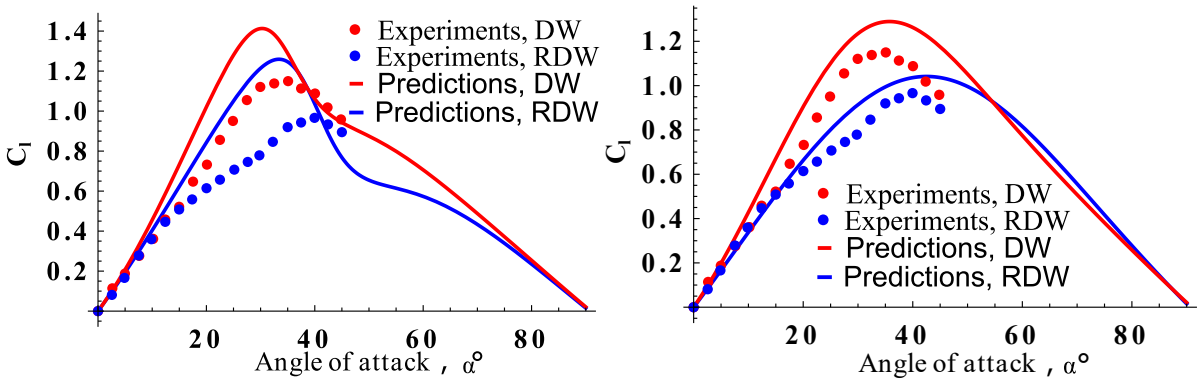

(a) $\sigma_1 = 0.3$.

(b) $\sigma_1 = 0.1$ for DW and 0.03 for RDW.

Figure 8. Predicted (solid lines) and measured lift coefficient (dots) for a delta wing (DW, red) and for a reversed delta wing (RDW, blue) with $AR = 1.86$. $\sigma_2 = \sigma_3 = 0.1$.

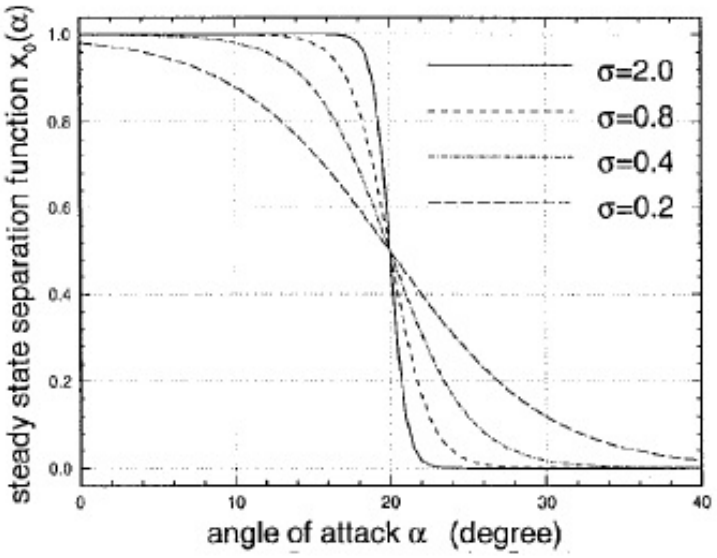

Figure 9. Change in the separation functions x as σ changes for a separation angle $\alpha^* = 20°$, (Fan and Lutze 1996).

If the results for the delta wing are general, the aerodynamic coefficients of tail fins in reverse flow are characterized by lower K_v and maximum lift, and a delay in stall as shown in Figure 8(b). These changes to K_v and other parameters are easily incorporated in the present model. There are, however, no data on RDW tail fin response with which to compare the model.

4 Mathematical Modeling of Tail Fins of High Aspect Ratio

Restricting the analysis to low AR delta wings restricts its applicability. As AR increases, however, the assumption of constant chordwise loading assumed in USBT is likely to become incorrect. At high AR, the load is high at the apex and decreases continuously to reach zero at the trailing edge where it satisfies the Kutta condition, (Lomax and Sluder 1951).

Different modifications have been suggested for USBT to account for the chordwise load variation, (Levin and Seginer 1982). One obvious method is to solve the Laplace equation for the three-dimensional potential function, rather than the two-dimensional form for USBT, Eqn. (2.2). The solution of the former, however, is very lengthy and will complicate the tail fin model developed here. A simpler model based on the method of R.T. Jones (see Chapter 13 of (Katz and Plotkin 2001)) as developed by (Traub 2003) is applied instead.

With larger AR, it is possible that the "added mass" becomes important. The model of (Traub 2003) assumes the apparent mass, m_c, of a high-AR delta wing to change as

$$\frac{dm_c}{dx} = 2\rho\pi c \tan^2\varepsilon \left(1 - \frac{x - x_p}{c_0}\sin\varepsilon\right) \tag{4.1}$$

where $\tan\varepsilon = b_0/(2c_0) = AR/4$: ε is related to the sweep angle by $\varepsilon = \pi/2 - \Lambda$, as shown in Figure 2a. The normal force derivative given by Eqn. (2.15) is scaled to high AR using the apparent mass:

$$\frac{dN_h}{dx} = \frac{dN}{dx}\left(1 - \frac{x - x_p}{c_0}\sin\varepsilon\right) \tag{4.2}$$

where the subscript "h" refers to high aspect ratio. The force and yaw moment for a high-AR tail fin is obtained from Eqns. (2.37) and (2.38) for the case of $x_p \gg c_0$ as

$$N_h = -0.5\rho A_{tf}\left[\left(\frac{1}{3} - \frac{1}{4}\sin\varepsilon\right)c_0 K_p \frac{\partial W}{\partial t} + x_1 K_p V_x W\right] - 0.5\rho A_{tf}\left[x_2 K_v + (1 - x_3)C_{Dc}\right]W^2 \tag{4.3}$$

and the yaw moment at the apex is

$$M_{a,h} = -0.5\rho A_{tf}\left[\left(\frac{1}{4} - \frac{1}{5}\sin\varepsilon\right){c_0}^2 K_p \frac{\partial W}{\partial t} + x_1 K_p x_{cp} c_0 V_x W\right] - \frac{2c_0}{3}0.5\rho A_{tf}\left[x_2 K_v + (1 - x_3)C_{Dc}\right]W^2 \tag{4.4}$$

where $\sin\varepsilon = AR/4/\sqrt{1 + (AR/4)^2}$. The closed-form steady force coefficients from (Traub 2003) become

$$K_p = \frac{\pi AR}{2}\left(1 - \frac{2}{3}\sin\varepsilon\right) \quad \text{and} \quad K_v = \frac{\pi AR}{2\sin\varepsilon}\left(1 - \frac{2}{3}\sin\varepsilon\right)\left(\frac{1}{2} + \frac{1}{3}\sin\varepsilon\right) \tag{4.5}$$

which is substituted in Eqns. (4.3) and (4.4). The authors assume that Eqn (4.5) holds for any delta fin. The center of pressure of potential flow moves toward the apex for a delta tail fin according to

$$x_{cp} = 1 - \frac{1 - \sin\varepsilon/2}{3 - 2\sin\varepsilon} \tag{4.6}$$

while the center of pressure of the vortex lift remains constant with AR.

The loss of lift for high AR (low Λ) is thought to be due to the vortex breakdown occurring at lower α as Λ decreases, (Traub 2003), as shown in Figure 4, and as found in modeling the flow over reverse delta wing in Section 3.1. (Traub 2003), however, modeled the loss in lift with increase AR as a reduction in $K_v = \pi/\exp(0.23(60 - \Lambda))$. As an alternative, we model the loss in lift as the AR increases in terms of a reduction in the transition angle of the vortex lift term α_2^* and a reduction in σ_2.

5 General Tail Fin Dynamic Equations

In this Section, the full aerodynamic equations for the normal force, N, and moment at the apex, M_a, of tail fins of any planform and aspect ratio are given. We will relax the assumption of W constant with respect to x and quantify its variation. Eqns. (2.15) and (2.16) are used for potential flow, and the effect of vortex and separated flow is added from Eqns. (2.37) and (2.38). The effect of vortex dynamics and high-AR scaling are added:

$$N = -\frac{\pi\rho}{4}\int_{x_p}^{x_p+c_0}\left[b^2\frac{\partial W}{\partial t}+V_x x_1\frac{\partial W(x,t)b^2(x)}{\partial x}\right]\left(1-\frac{x-x_p}{c_0}\sin\varepsilon\right)dx- \\ \frac{\rho}{2}\left[x_2K_v+(1-x_3)C_{Dc}\right]\int_{x_p}^{x_p+c_0}b(x)W^2dx \quad (5.1)$$

and the yaw moment at the tail fin apex as

$$M_a = -\frac{\pi\rho}{4}\int_{x_p}^{x_p+c_0}\left[b^2\frac{\partial W}{\partial t}+V_x x_1\frac{\partial W(x,t)b^2(x)}{\partial x}\right]\left(1-\frac{x-x_p}{c_0}\sin\varepsilon\right)(x-x_p)dx- \\ \frac{\rho}{2}\left[x_2K_v+(1-x_3)C_{Dc}\right]\int_{x_p}^{x_p+c_0}b(x)(x-x_p)W^2dx \quad (5.2)$$

These integral equations can have an analytic form, as will be shown in Section 13.3.

6 Elliptic Tail Fin Modeling

The analysis so far has considered only a delta planform. In this section the yaw moment equation is derived for the elliptic tail fin shown in Figure 2b. An elliptical planform, or indeed any planform where $b(x)$ goes smoothly to zero at the trailing edge, is surprisingly difficult to accommodate in USBT. The reason is that the approximate right side of Eqn (2.15) when $db(x)/dx < 0$ will give no contribution to the force or moment. Only the half-section of the ellipse closest to the rotor generates force and moment in the linear model. The effects of the nonlinear LEV, however, extend beyond the maximum $b(x)$, generating what (Lamar 1976b) called "augmented vortex lift" on the aft section, as shown in Figure 10 for a cropped delta wing, (Lamar 1976b).

It will be assumed that the potential force distribution over the ellipse surface is linear with the chord, $c(x)$. Further, the high aspect ratio correction has the form used for the triangular tail fin in Eqn. (4.2). The integrated form of the Eqns. (5.1) and (5.2) will be derived in Section 8.1.1. Only the basic features of elliptical tail fin will be stated in this section.

The width of the elliptical tail fin is given by

$$b(x) = 2b_0\sqrt{\frac{c(x)}{c_0} - \frac{c^2(x)}{c_0^2}} \tag{6.1}$$

For an elliptical tail fin, the apex angle is $\sin\varepsilon = \pi AR/4/\sqrt{1+(\pi AR/4)^2}$, and $AR = 4b_0/(\pi c_0)$.$K_p = \pi AR/2$ for low AR and

$$K_p = \pi AR(1-\sin\varepsilon/3)/2 \tag{6.2}$$

for high aspect ratio. The change of K_p for an elliptic planform with AR using three-dimensional calculations due to (Krienes 1941) and taken from (Cohen and Jones 2015) is shown in Figure 11. The variation in K_p of the equation given above agrees very well with those of (Krienes 1941) in Figure 11.

The variation in the center of pressure assuming linear chordwise potential load distribution as in Section 4, gives

$$x_{cp} = \left(\frac{1}{2} - \frac{1-\sin\varepsilon/4}{3-\sin\varepsilon}\right)c_0 \tag{6.3}$$

so that x_{cp} moves rearward as AR increases. Contrarily, for an elliptical wing, x_{cp} moves forward as AR increases as shown using three-dimensional potential flow calculations in (Krienes 1941).

An exact solution for aerodynamic loads on an elliptical wing is derived in (Hauptman and Miloh 1986). A simpler fitting to the x_{cp} data for potential flow over an elliptical wing in (Krienes 1941) and shown in Figure 12 is:

$$x_{cp} = 0.12(2.35 - \exp(-0.94AR)) \tag{6.4}$$

while the center of pressure of the vortex load is assumed to be at the center of the ellipse, $c_0/2$, and is independent of AR.

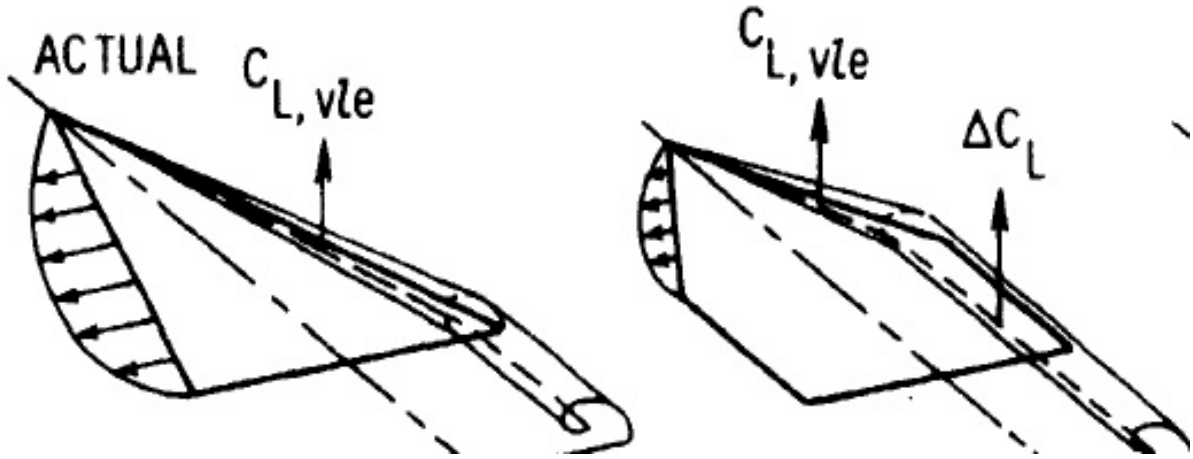

Figure 10. Vortex lift $C_{Lv,le}$ and augmented vortex lift, ΔC_L for a cropped delta wing, (Lamar 1976b).

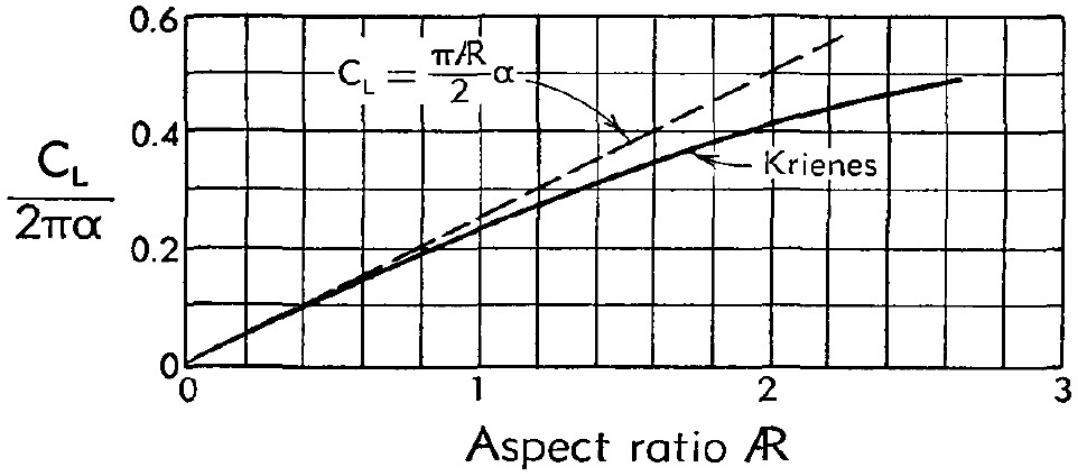

Figure 11. Comparison of lift curve slope for wings of low aspect ratio, $K_p = C_L$, with Eqn. (6.2) (solid line), (Cohen and Jones 2015).

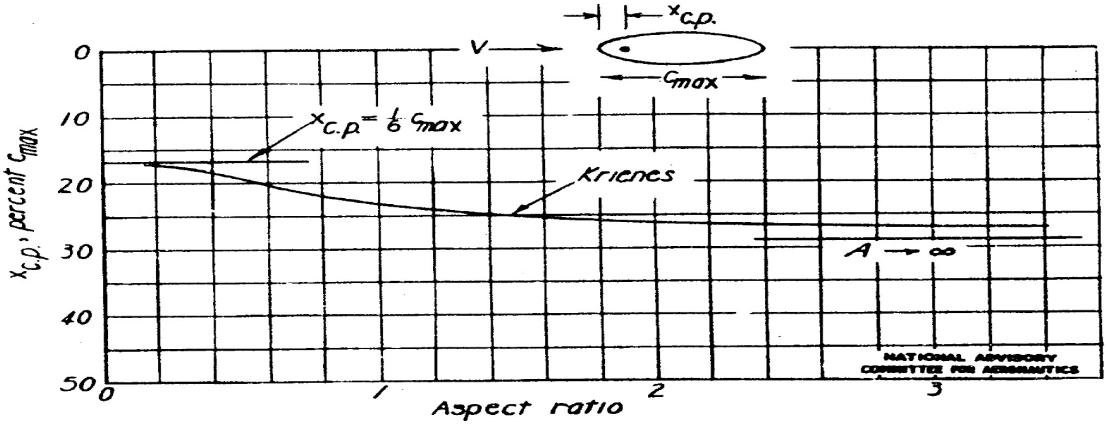

Figure 12. Comparison of center of pressure given by theory for wings of low aspect ratio with results given by Krienes (Krienes 1941) for an elliptical wing.

7 Rectangular Tail Fin Modeling

The problem of using USBT for a rectangular tail fin is an extension of that discussed above for an ellipse: USBT concentrates the load at the leading-edge, whereas it has been shown that the loading is distributed (Lomax and Sluder 1951). Another issue with rectangular planforms is the generation of side edge vortices in addition to those on the leading-edge. Both of these issues are demonstrated in Figure 13. USBT can still can be used to predict the apparent inertia and aerodynamic damping terms if the loading distribution is estimated accurately.

(Lomax and Sluder 1951) derived a correction function for chordwise loads over triangular and rectangular wings of low AR. This function, however, can only be integrated numerically. As an alternative, we reuse the assumption made for the delta and elliptical planforms: the loading is linear with chord, as in Eqn. (4.2). This linear distribution is scaled with an AR term that vanishes as $AR \downarrow 0$. For the steady state term, a relation for K_p that fits the analysis in (Lomax and Sluder 1951) was derived by (Helmbold 1942) and restated in many references, for instance, (Lamar 1974), as

$$K_p = \frac{2\pi AR}{2+\sqrt{AR^2+4}} \tag{7.1}$$

where, $AR = b_0/c_0$. On a rectangular tail fin, the center of pressure of moves forward with increasing AR as shown in Figure 14, which is the same direction as for swept wings, (Hopkins 1951), but the opposite direction for a delta fin. From (Lomax and Sluder 1951), the change in x_{cp} is given by

$$x_{cp} = 0.25\Big(1-\exp(-AR)\Big) \tag{7.2}$$

A curve fitting of x_{cp} as a function of AR for unswept wings is given in (Barnes and Barnes 1997), but Eqn. (7.2) should be more accurate for rectangular wings based on the results of (Lomax and Sluder 1951) and (Lawrence 1951).

The other issue of side edge vortices and their effect on the value of K_v has been investigated thoroughly in (Lamar 1974) for rectangular and swept wings with sharp side edges and different ARs. K_v from the LEV and side edge vortices was found to be $K_v = \pi \pm 0.1$ for all AR, as shown in Figure 7 for a rectangular wing. The LEV coefficient $K_{v,le}$ and the side edge vortex coefficient $K_{v,se}$ can be determined from the following relations for a rectangular wing, (Larson 1981):

$$K_{v,le} = \frac{\pi AR}{2\left(1+\sqrt{1+AR^2/16}\right)} \tag{7.3}$$

$$K_{v,se} = 2\pi/(AR+2) \tag{7.4}$$

and $K_v = K_{v,le} + K_{v,se}$.

Applying the above modifications to the USBT yields the relations for the force and yaw moment of a rectangular tail fin as will be shown in Section 8.1.1.

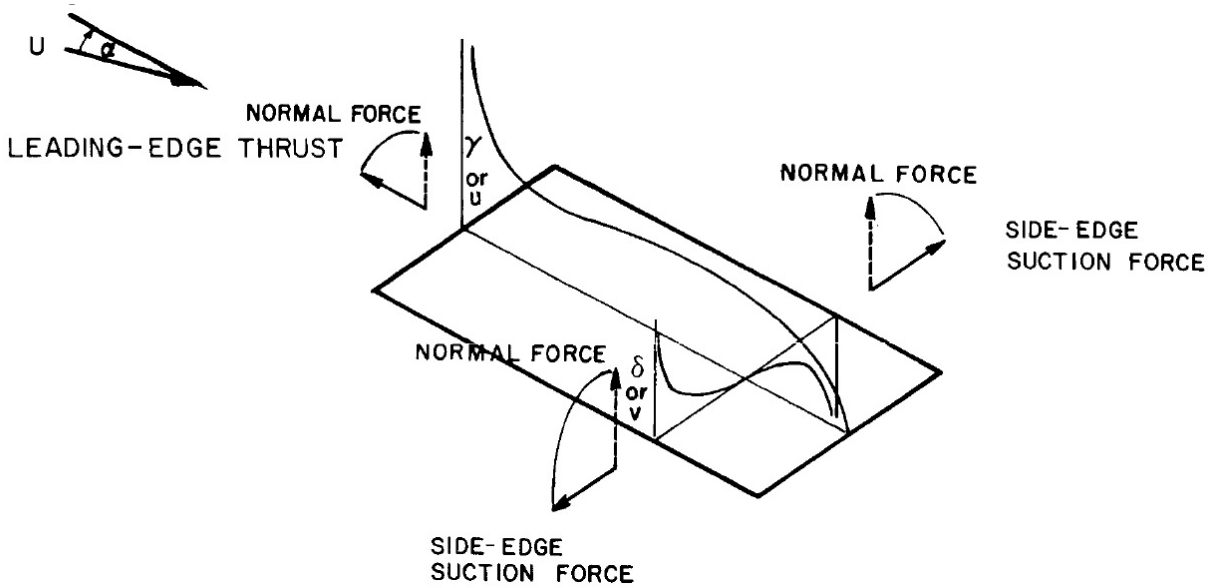

Figure 13. Chordwise load variation over a rectangular wing and the normal forces due to the LEV and side edges vortices, (Lamar 1974).

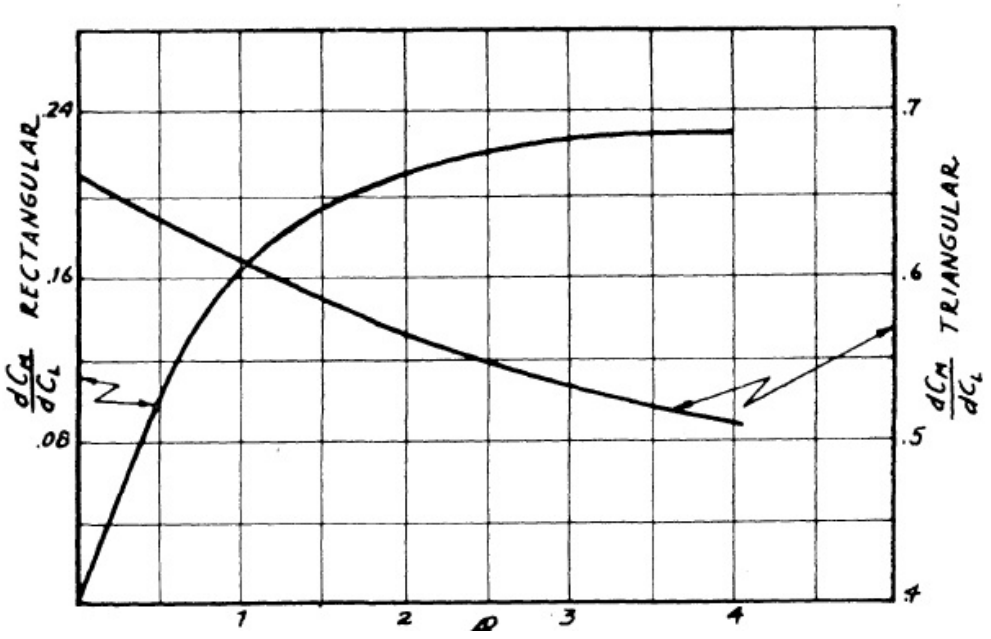

Figure 14. Variation of the enter of pressure with AR of rectangular and delta (labelled "triangular") planforms from (Lawrence 1951).

8 Mathematical Model Validation

This section describes the validation of the different forms of the tail fin model using data obtained in the large wind tunnel of the University of Perugia, under the direction of Professor Francesco Castellini. The results have yet to be published and are used here with his permission. The experiments were done at nominal wind speeds of 5, 10, and 17 m/s. Tail fins of the three planforms analyzed here, and varying AR, were investigated. To simplify the comparison, the wind tunnel models did not have a nacelle and rotor. The geometry of the tail fins is given in Table 1. The first three rows show the low$-AR$ tail fins and the second three the higher AR ones. Table 2 documents the model constants used in the simulations. All the fins were released at two initial yaw angles: $\gamma_0 = -40^\circ$ and -80°, and their subsequent motion recorded. The sign of the angle is not significant – so "high" will refer to magnitude – but is included for consistency with the experiments. High release angles, for which nonlinear effects should be important, have not been measured previously nor has the response at different wind speeds.

Table 1. Geometry of the tail fins. $x_p = 0.443$ m for all fins, and I_z is with respect to the yaw axis.

Planform	AR	c_0 (m)	b_0 (m)	I_z (kgm^2)
delta	0.58	0.27	0.078	0.06
elliptical	0.37	0.27	0.078	0.044
rectangular	0.5	0.143	0.072	0.038
delta	1.97	0.143	0.141	0.04
elliptical	1.25	0.143	0.141	0.04
rectangular	2.03	0.07	0.142	0.034

Because the tail fins in these experiments rotated about the yaw axis, we now consider moments about this axis, M_z, which is the origin for x in Figure 1.

In view of the complexity of the nonlinear yaw equations, we now establish the importance of the nonlinearity, which should be most apparent at large yaw and high aspect ratios. Figure 15(a) compares the response of the delta fin with the highest $AR = 1.97$ for the two release angles, in terms of $\gamma(t)/\gamma_0$ against time, t. Only 200 data points out of 4000 for the 4 s time interval, for $\gamma_0 = -40^\circ$ are plotted to allow for easy comparison. If the two responses were governed by the same linear equation, this scaling would collapse the two responses, which is obviously not the case in part (a). What is most noticeable is that the first zero crossing is reached considerably more quickly for $\gamma_0 = -40^\circ$, after which the frequency of the response is approximately independent of γ_0. This is made clearer in part (b) where the responses are rescaled by γ_{max}, the first maxima in $\gamma(t)$; $\gamma_{max} = 46.82^\circ$ at $t_{max} = 0.493$ s and 17.30° at $t_{max} = 0.389$ s for $\gamma_0 = -80^\circ$ and -40°, respectively, and the x-axis shows $t - t_{max}$. The results now collapse, showing the nonlinear terms in the moment equations are needed only for $\gamma(t)$ higher than about 45°. We do not show any further results in the interest of brevity, but resetting γ_{max} to subsequent local maxima for each γ_0 gives a collapse in γ/γ_{max} similar to that shown in part (b). Thus, the ability of the nonlinear models to predict the initial yaw response for $\gamma_0 = -80^\circ$ is a particularly important test of their accuracy.

A further development is noted, but not described, as is not directly relevant to the aim of this report. The authors have derived an approximate analytical solution for yaw response. This solution is based on approximating the nonlinear terms by a fifth-degree polynomial in γ using the Chebyshev series. The series, however, is accurate only for $90^\circ \geq \gamma \geq 45^\circ$. To get an accurate solution for $\gamma_0 \leq 45^\circ$, the solution is considered to be a function of the range of γ by scaling γ by γ_0 to place it within the best range for approximation by the Chebyshev series.

Table 2. Model constants. $C_{Dc} = 1.3, \sigma_1 = 0.3$, and $\sigma_2 = \sigma_3 = 0.1$ for all fins. Note that x_{cp} is given as a fraction of c_0.

Planform	AR	K_p	K_v	x_{cp}	$\alpha_1^*(^\circ)$	$\alpha_2^*(^\circ)$	$\alpha_3^*(^\circ)$
delta	0.58	0.911	π	0.667	39	60	60
elliptical	0.37	0.581	π	0.167	38	55	60
rectangular	0.5	0.785	2.9	0.098	39	55	60
delta	1.97	2.078	π	0.625	33	38	38
elliptical	1.25	1.505	π	0.245	15	20	25
rectangular	2.03	2.630	π	0.217	20	20	25

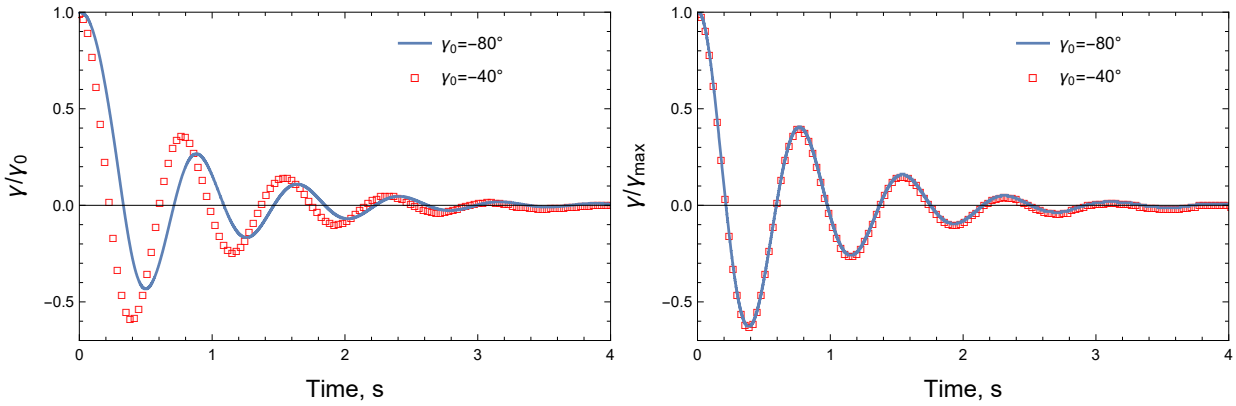

(a) Full response for $\gamma_0 = -40°$ (□) and $-80°$ (solid line). Only a selection of the $-40°$ results are shown.

(b) Response rescaled by γ_{max}, the first maxima in $\gamma(t) = 46.82°$ and $17.3°$ for $\gamma_0 = -40°$ and $-80°$ respectively.

Figure 15. Comparison of the yaw response of a delta tail fin of $AR = 1.97$ for the two release angles. $U = 17$ m/s.

The final tests were made for an unsteady U of sinusoidal form, which also has not been done previously. The final novelty of the experiment was the determination of the frictional torque in the yaw bearings, so its effects on the present model could be quantified. This is postponed to Section 9 because bearing friction was only important for $U = 5$ m/s, as demonstrated by the one presentation of these results in this section. The remaining results, for $U = 10$ and 17 m/s, were simulated by ignoring friction.

8.1 Validation of the Model for Low-Aspect-Ratio Tail Fins

In this section the modeled response of the delta, elliptical, and rectangular tail fins of low aspect ratios are compared with the measurements.

8.1.1 Delta Tail Fins

The simplest test of the tail fin is a comparison with the steady wind tunnel experiments for the low-aspect-ratio tail fin of $AR = 0.58$ whose geometry is listed in Table 1. The test conditions were $U = 17$ m/s, and $\gamma_0 = -40°$. The delta tail fin moment of inertia around the yaw axis, I_z, was determined from (Singh, Hemmati, and Wood 2012) as

$$I_z = m\left(x_p^2 + \frac{1}{2}c_0^2 + \frac{4}{3}x_p c_0\right) \tag{8.1}$$

where m is the mass. This equation is valid for a sheet-metal fin of constant thickness. For all the wind tunnel tests, $V_{in} = V_{x,el} = 0$ and $V_{y,el} = -\dot{\gamma}(x_p + c(x))$. Note that $c_0 \approx x_p$, which holds for all three planforms considered in this section, so the variation in W must be considered: $dW/dx = \dot{\gamma}$. Also, $\beta = \gamma$ and $\dot{U} = 0$, except in Section 8.3 where varying wind speed is considered. By changing the integration for the moment equation to be from $x = 0$ to $x_p + c_0$, we determine M_z as

$$\begin{aligned} M_z = I_z\ddot{\gamma} = -0.5\rho A_{tf}\Bigg[&\left(\left(\frac{1}{5} - \frac{1}{6}\sin\varepsilon\right)c_0^3 + \left(\frac{1}{2} - \frac{2}{5}\sin\varepsilon\right)x_p c_0^2 + \left(\frac{1}{3} - \frac{1}{4}\sin\varepsilon\right)x_p^2 c_0\right)K_p\ddot{\gamma} + \\ &Ux_1\cos\gamma\left(\left(1 - \frac{4}{5}\sin\varepsilon\right)c_0^2 + \left(2 - \frac{3}{2}\sin\varepsilon\right)x_p c_0 + \left(1 - \frac{2}{3}\sin\varepsilon\right)x_p^2\right)K_p\dot{\gamma} + \\ &U^2 x_1\cos\gamma(x_p + x_{cp})K_p\sin\gamma + \left(\left(\frac{1}{4} - \frac{1}{5}\sin\varepsilon\right)c_0{}^2 + \left(\frac{1}{3} - \frac{1}{4}\sin\varepsilon\right)x_p c_0\right)K_p\dot{U}\sin\gamma\Bigg] - \\ &0.5\rho A_{tf}\Bigg[2U\left(\frac{1}{2}c_0^2 + \frac{4}{3}x_p c_0 + x_p^2\right)(x_2K_v + (1-x_3)C_{Dc})|\sin\gamma|\dot{\gamma} + \\ &\left(\frac{2}{5}c_0^3 + \frac{3}{2}x_p c_0^2 + 2x_p^2 c_0 + x_p^3\right)(x_2K_v + (1-x_3)C_{Dc})|\dot{\gamma}|\dot{\gamma} + \\ &\left(x_p + \frac{2c_0}{3}\right)\left(x_2K_v|\sin\gamma| + (1-x_3)C_{Dc}\right)U^2\sin\gamma\Bigg] \end{aligned} \tag{8.2}$$

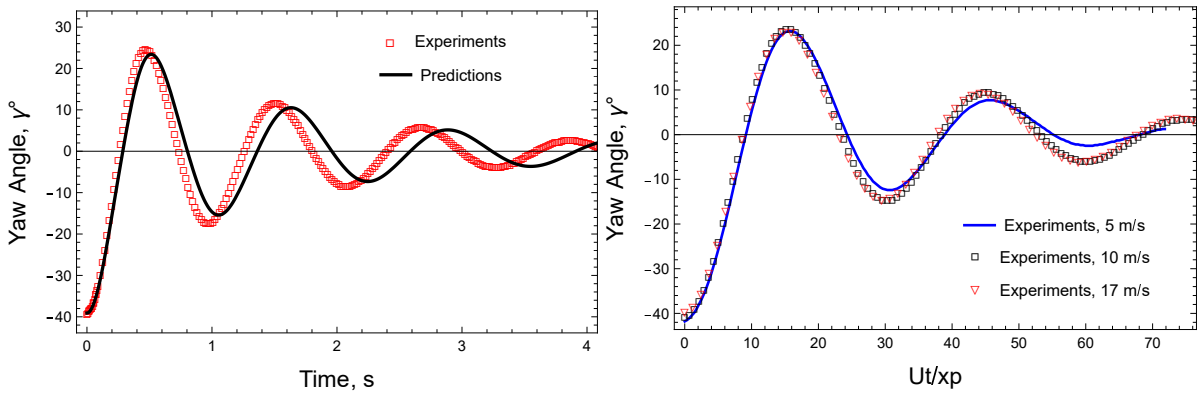

(a) Yaw angle predictions (black line) compared to the measurements (red □). $U = 17$ m/s.

(b) Measured responses against Ut/x_p for 17 m/s (black dots), 10 m/s (in red) and 5 m/s (in blue).

Figure 16. Yaw response of a delta tail fin of $AR = 0.58$, and $\gamma_0 = -40°$.

where $K_p = \pi AR/2$, and $A_{tf} = b_0 c_0/2$. K_p, K_v were determined from Eqn. (4.5), and x_{cp} from Eqn. (4.6). For this low $AR < 1$, the high-AR corrections were neglected and $\sin\varepsilon \approx 0$ was assumed in Eqn. (8.2). The model constants are collected in Table 2, and the results are shown in Figure 16(a). Eqn. (8.2) is formatted to show the linear terms, containing K_p but not K_v, in the first three lines. The fist term on the third line is the steady term due to potential flow, which is linearized when $\sin\gamma \approx \gamma$, and the second is the unsteady wind speed term considered in Section 8.3. The nonlinear vortex terms involving K_v are in the last three lines. This formatting is also used below for the other planforms.

On purely dimensional grounds, the frequency of the yaw response for any planform is directly proportional to U, as seen in the measured responses at wind speeds of $U = 17, 10$, and 5 m/s in Figure 16(b). Damping, however, increases slightly for $U = 5$ m/s as a result of the increasing effect of bearing friction as U decreases. Friction is considered in detail in Section 9, where we analyze the steady state error (γ at $\dot{\gamma} = 0$) at large t.

The predictions for the higher $\gamma_0 = -80°$ and the experimental results are compared in Figure 17. There is some discrepancy in the frequency throughout the response, even as α decreases to values where vortex lift is not likely to be important. In Section 10, system identification of the x-function parameters will be shown to give to better fit to the measurements.

Elliptical Tail Fins

An elliptical tail fin of low aspect ratio $AR = 0.37$ is compared to the measurements for $\gamma_0 = -40°$ and $-80°$ in Figure 18. The tail fin geometry is documented in Table 1. The tail fin moment of inertia around the yaw axis is calculated as in (Singh, Hemmati, and Wood 2012) as

$$I_z = m\left(x_p^2 + \frac{5}{16}c_0^2 + x_p c_0\right) \tag{8.3}$$

The tail fin boom combined moment of inertia around the yaw axis is listed in Table 1. The vortex force of an elliptical tail fin is assumed to act over the entire fin, as discussed in Section 6. Using Eqn. (5.2), with the potential flow integral limits being $x = 0$ and $x = x_p + c_0/2$, and the vortex flow ones $x = 0$ and $x = x_p + c_0$, the moment equation

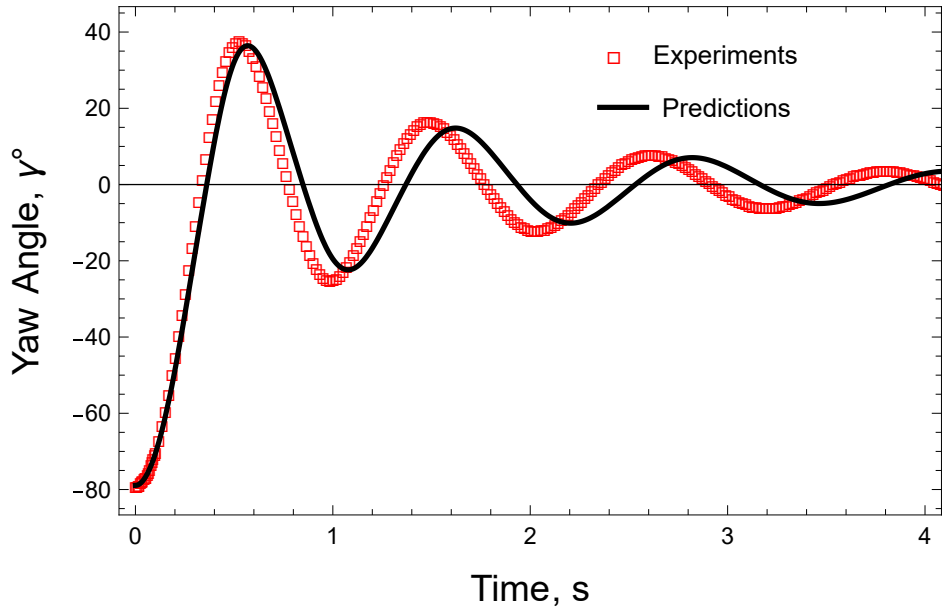

Figure 17. Yaw angle predictions (black line) compared to the experimental results (red □) for a delta wing tail fin of $AR = 0.58, U = 17$ m/s and $\gamma_0 = -80°$.

for an elliptical tail fin is

$$
\begin{aligned}
I_z\ddot{\gamma} = -0.5\rho A_{tf}\Bigg[& \left(\left(\frac{3}{80} - \frac{7}{480}\sin\varepsilon\right)c_0^3 + \left(\frac{5}{24} - \frac{3}{40}\sin\varepsilon\right)x_p c_0^2 + \left(\frac{1}{3} - \frac{5}{48}\sin\varepsilon\right)x_p^2 c_0\right)K_p\ddot{\gamma} + \\
& U x_1 \cos\gamma\left(\left(\frac{1}{4} - \frac{7}{80}\sin\varepsilon\right)c_0^2 + \left(1 - \frac{7}{24}\sin\varepsilon\right)x_p c_0 + \left(1 - \frac{5}{6}\sin\varepsilon\right)x_p^2\right)K_p\dot{\gamma} + \\
& U^2 x_1 \cos\gamma(x_p + x_{cp}c_0)K_p\sin\gamma + \left(\left(\frac{5}{48} - \frac{3}{80}\sin\varepsilon\right)c_0{}^2 + \left(\frac{1}{3} - \frac{5}{48}\sin\varepsilon\right)x_p c_0\right)K_p\dot{U}\sin\gamma\Bigg] - \\
& 0.5\rho A_{tf}\Bigg[2U\left(\frac{5}{16}c_0^2 + x_p c_0 + x_p^2\right)(x_2 K_v + (1-x_3)C_{Dc})|\sin\gamma|\dot{\gamma} + \\
& \left(\frac{7}{32}c_0^3 + \frac{15}{16}x_p c_0^2 + \frac{3}{2}x_p^2 c_0 + x_p^3\right)(x_2 K_v + (1-x_3)C_{Dc})|\dot{\gamma}|\dot{\gamma} + \\
& \left(x_p + \frac{c_0}{2}\right)\left(x_2 K_v|\sin\gamma| + (1-x_3)C_{Dc}\right)U^2\sin\gamma\Bigg] \qquad (8.4)
\end{aligned}
$$

where K_p, K_p, and x_{cp} are given in Table 2, and $A_{tf} = \pi b_0 c_0/4$.

The separation angles α^* for the elliptic tail fins are based on those of a delta wing that is circumscribed by the front half of the ellipse. For the current ellipse, this is equivalent to $\Lambda = 75°$. $\alpha_1^* = 38°$ while $\alpha_2^* = 55°$ and $\alpha_3^* = 60°$. The small AR tail was tested at $\gamma_0 = -40°$ and $U = 10$ m/s, Figure 18(a). For $U = 17$ m/s and $\gamma_0 = -80°$, the results are shown in Figure 18(b). The accuracy of the model at high γ_0, which increases the nonlinearity of the response, is comparable to that at $\gamma_0 = -40°$.

Rectangular Tail Fins

The yaw moment of inertia of the rectangular tail fin from (Singh, Hemmati, and Wood 2012) is

$$I_z = m\left(x_p^2 + \frac{1}{3}c_0^2 + x_p c_0\right) \qquad (8.5)$$

The rectangular tail fin dimensions are listed in Table 1. The test conditions were $U = 17$ m/s, and $\gamma_0 = -80°$.

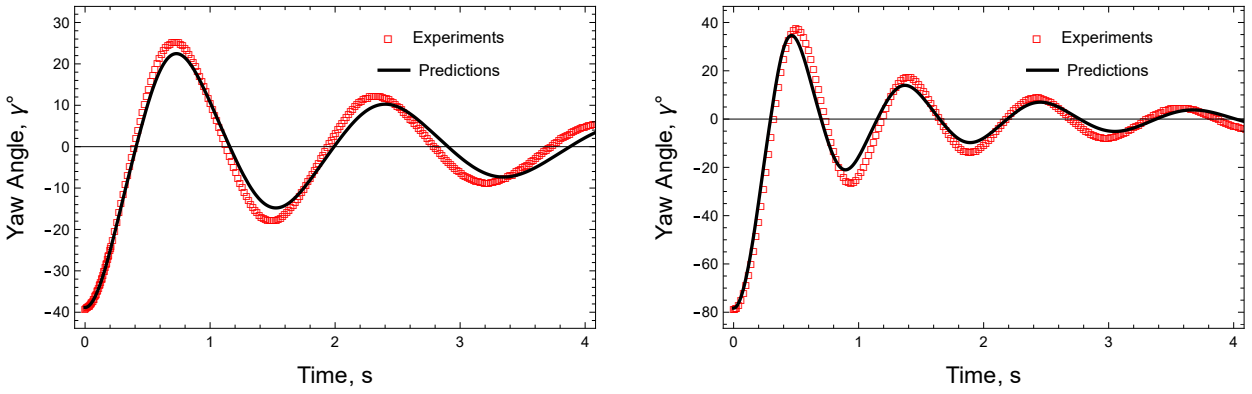

(a) $U = 10$ **m/s and** $\gamma_0 = -40°$. **(b)** $U = 17$ **m/s and** $\gamma_0 = -80°$.

Figure 18. Yaw angle predictions of an elliptical tail fin using nonlinear analyses Eqn. (8.4) (black line) compared to the experimental results (red □). $AR = 0.37$.

The moment equation for a rectangular tail fin from Eqn. (5.2) is

$$
\begin{aligned}
I_z\ddot{\gamma} = -0.5\rho A_{tf}\Bigg[& \left(\left(\frac{1}{3}-\frac{1}{4}\sin\varepsilon\right)c_0^3+\left(1-\frac{2}{3}\sin\varepsilon\right)x_p c_0^2+\left(1-\frac{1}{2}\sin\varepsilon\right)x_p^2 c_0\right)K_p\ddot{\gamma}+ \\
& Ux_1\cos\gamma\left(\left(1-\frac{2}{3}\sin\varepsilon\right)c_0^2+(2-\sin\varepsilon)x_p c_0+x_p^2\right)K_p\dot{\gamma}+ \\
& U^2 x_1\cos\gamma(x_p+x_{cp}c_0)K_p\sin\gamma+\left(\left(\frac{1}{2}-\frac{1}{3}\sin\varepsilon\right){c_0}^2+\left(1-\frac{1}{2}\sin\varepsilon\right)x_p c_0\right)K_p\dot{U}\sin\gamma\Bigg]- \\
& 0.5\rho A_{tf}\Bigg[2U\left(\frac{1}{3}c_0^2+x_p c_0+x_p^2\right)(x_2K_v+(1-x_3)C_{Dc})|\sin\gamma|\dot{\gamma}+ \\
& \left(\frac{1}{4}c_0^3+x_p c_0^2+\frac{3}{2}x_p^2 c_0+x_p^3\right)(x_2K_v+(1-x_3)C_{Dc})|\dot{\gamma}|\dot{\gamma}+ \\
& \left(x_p+\frac{c_0}{2}\right)\left(x_2K_v|\sin\gamma|+(1-x_3)C_{Dc}\right)U^2\sin\gamma\Bigg] \qquad (8.6)
\end{aligned}
$$

where K_p, K_v, and x_{cp} are defined in Section 7 and Table 2, and $A_{tf} = b_0 c_0$. A delta wing of the same dimensions has $AR = 1$, $\alpha_1^* = 39°$ from (Okamoto and Azuma 2011) while $\alpha_2^* = 55°$, $\alpha_3^* = 60°$ from Figure 4. These values were used to obtain the results shown in Figure 19. The model reproduces the experimental damping but underpredicts the frequency of the response, probably because of the inappropriate use of the separation angles for a delta wing. We could not find independent values for rectangular planforms. Section 13.2 shows that improved fitting of data is possible using system identification.

8.2 Validation of the Model for High-Aspect-Ratio Tail Fins

In this section, the model for $AR > 1$ is validated against experiments. The three cases are listed in the last three rows of Table 1. For the model, the tail fin parameters in Table 2 were chosen as described above with σ_1, σ_2, and σ_3 retaining their low-AR values. For the delta tail fin: $\alpha_1^* = 33°$, and $\alpha_2^* = \alpha_3^* = 38°$. Results for the delta tail fin of $AR = 1.97$ at $U = 17$ m/s, and $\gamma_0 = -40°$ are shown in Figure 20(a), and for the higher $\gamma_0 = -80°$ in Figure 20(b). The theory is, surprisingly, more accurate than for $\gamma_0 = -40°$, which implies that the modeling of the nonlinear effects at high α is accurate.

Figure 21 shows the results for elliptic tail fin of $AR = 1.25$ compared to the experiments for $U = 17$ m/s. The separation angles for this equivalent delta wing of $\Lambda = 45°$ are $\alpha_1^* = 15°$, which was taken to be the stall angle for a delta wing of $AR = 4$ from (Okamoto and Azuma 2011), and $\alpha_2^* = 20°$ and $\alpha_3^* = 25°$ from extrapolating the curves in Figure 4. The good agreement is particularly important it implies the validity of the USBT requirement that the rear half of the tail fin with decreasing $c(x)$ does not contribute to the yaw dynamics of potential flow. If this result is general, then it has significant implications for the design of tail fins. The response at high release angle of $-80°$ is shown in Figure 21(b) to be as good as for the lower γ_0.

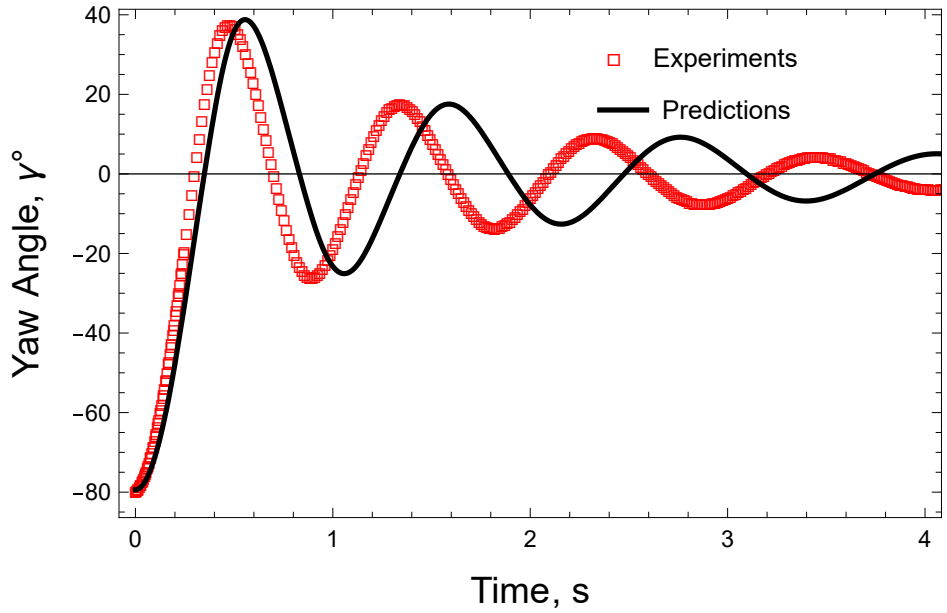

Figure 19. Yaw angle predictions Eqn. (8.6) (black line) compared to the experimental results (red □) of a rectangular tail fin of $AR = 0.5, U = 17$ m/s and $\gamma_0 = -80°$.

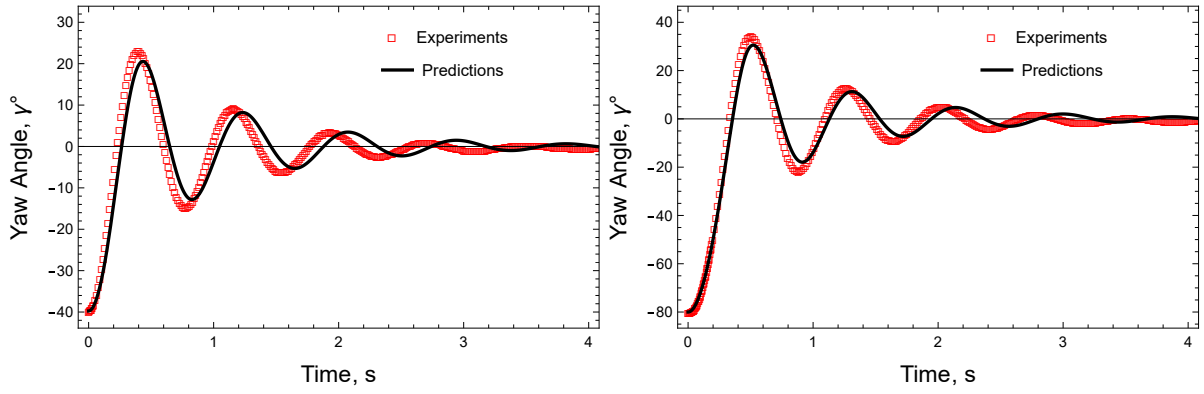

(a) $\gamma_0 = -40°$. **(b)** $\gamma_0 = -80°$.

Figure 20. Yaw angle predictions for a delta tail fin using nonlinear analyses Eqn. (8.2) (black line) compared to the experimental results (red □) for a delta fin. $AR = 1.97, U = 17$ **m/s.**

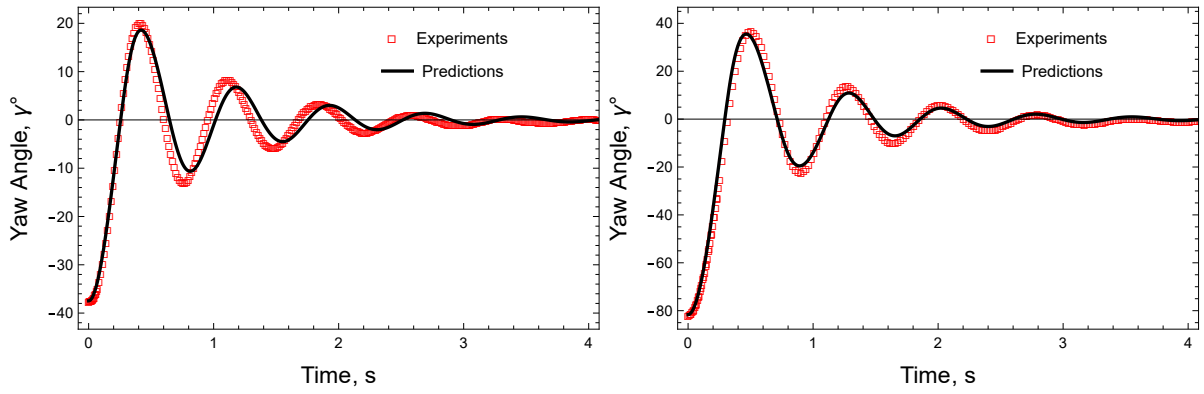

(a) $\gamma_0 = -40°$. **(b)** $\gamma_0 = -80°$.

Figure 21. Yaw angle predictions for an elliptic tail fin using nonlinear Eqn. (8.4) (black line) compared to the experimental results (red □). $AR = 1.25, U = 17$ **m/s.**

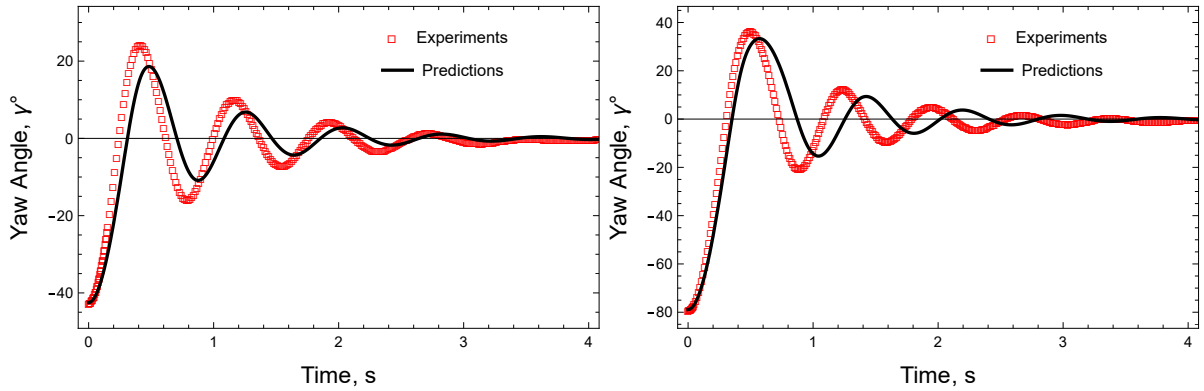

(a) $\gamma_0 = -40°$. **(b)** $\gamma_0 = -80°$.

Figure 22. Yaw angle predictions for a rectangular tail fin using nonlinear Eqn. (8.6) (black line) compared to the experimental results (red □). $AR = 2.03, U = 17$ **m/s.**

The high-AR rectangular tail fin results are shown in Figure 22(a). for this case $AR = 2$, and the equivalent delta wing $AR = 4$. From (Okamoto and Azuma 2011), $\alpha_1^* = 20°$, whereas $\alpha_2^* = 20°$ and $\alpha_3^* = 25°$ from Figure 4, and $K_{vse} = 1.57$, and $K_{vle} = 1.5$. The model overpredicts the damping and the frequency, with the latter being more apparent in Figure 22(b) for the higher γ_0. This especially severe case is investigated further in Section 13 where the response is recalculated with the α^* and σ model parameters determined from system identification.

8.3 Unsteady Wind Speed

The full dynamic equations for all planforms have a term in dU/dt, but, as far as the authors are aware, no unsteady wind speed yaw response experiments have been undertaken. The reason may well be that it is difficult to produce a consistent unsteady flow in a wind tunnel, but fortunately the tunnel at the University of Perugia does allow limited, low-frequency variations. The experimental responses considered in this section were made at the highest available frequency and amplitude of the (sinusoidal) variations. Tail fins of the three planforms shapes were tested at different mean wind speed of different amplitudes to cover high and low U. The frequency of wind speed for all the tests was $\omega = 0.63$ rad/s, so the wind speed is given by

$$U(t) = U_m + U_a \sin(\omega t + \phi) \tag{8.7}$$

where $U_m = 9.86$, $U_a = 1.5$ m/s, and the phase angle $\phi = 120°$. The response of the $AR = 1.97$ delta fin is shown in Figure 23, together with that from neglecting the $\dot{U}$ term in Eqn. (8.2). The origin for t in Eqn. (8.7) is also the origin in Figure 23. The figure shows that the unsteady wind speed effect is negligible. Given that the frequency and amplitude of wind speed changes in practice can greatly exceed the changes available in the wind tunnel, it is important to include the unsteady-U terms to maximize the accuracy of the predictions. It is likely that assessing the accuracy of modeling tail fin response to unsteady winds will require field measurements of SWT yaw behavior.

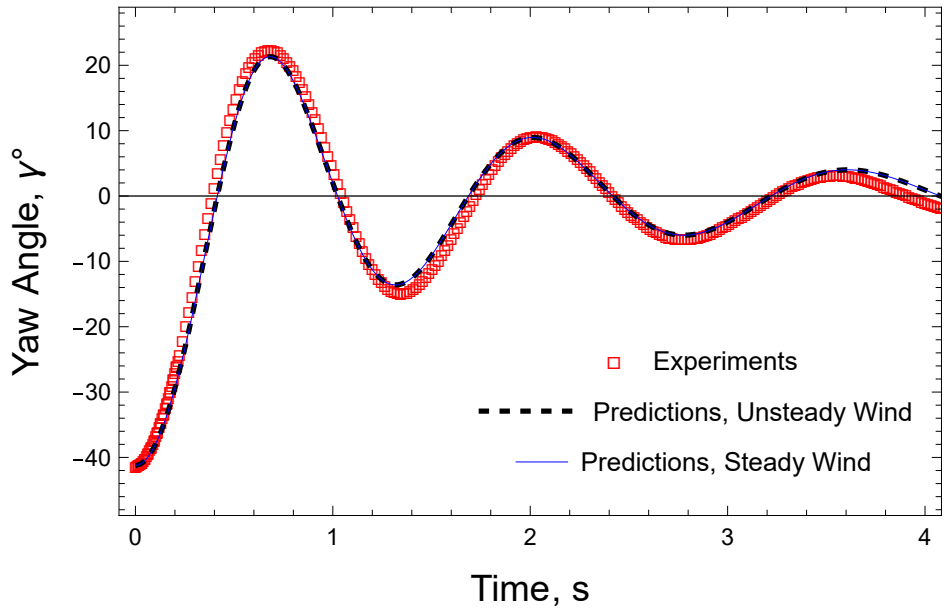

Figure 23. Yaw angle predictions of the delta wing fin using nonlinear Eqn. (8.2) for unsteady wind speed given by Eqn. (8.7) (black dashed line) and for steady U (blue line), and the experimental results (red □). $AR = 1.97$, $U_m = 9.86$ **m/s,** $U_a = 1.5$ **m/s,** $\omega = 0.63$ **rad/s,** $\phi = 120°$ **and** $\gamma_0 = -40°$.

9 The Effects of Yaw Bearing Friction

The theory developed so far has ignored the effects of yaw bearing friction, which may be important for SWTs and tail fin models tested in wind tunnels. To date, no tail fin experiment has considered the frictional resistance, and there is little information in the literature about the effects of bearing friction on SWT performance in general. The only studies known to the authors, (Vaz et al. 2018; Moreira et al. 2020), focused on the effects of drivetrain friction on the starting performance of a model SWT that did not yaw.

Equation (27) of the simplified loads model in the standard for SWTs, (IEC 2013), gives the maximum yaw rate as 3 rad/s, which corresponds to around 30 rpm. This is a low angular velocity for a bearing. Friction modeling for bearings is complex in general, e.g., (SKF 2023) and so the present analysis will consider only low angular velocities and will ignore any differences between γ as defined here, and the corresponding value in the inertial x_i, y_i coordinates attached to the tower. The low-velocity assumption could not be made by (Vaz et al. 2018), and the reader is referred to that paper for more general details of bearing modeling.

The restriction to low angular speeds means the difference between static and dynamic friction must be considered because the former is usually significantly larger than the latter. The difference is due to the "Stribeck" effect, the lack of lubricant penetration between the rolling elements and the race of stationary bearings; a lubricant film is established only after the bearing has rotated for some time or has reached some minimum γ. It is to be expected, therefore, that a SWT that has not been yawing or rotating due to low wind speeds will experience significant static resistive torque in the drivetrain and yaw bearings as the wind picks up, but the subsequent yaw motion will be free of the Stribeck effect, even if the yaw rate goes through zero. The authors have not found any information on the time it takes a lubricant film to retreat from the contact zone between the rolling elements and race once a bearing has stopped rotating. In the wind tunnel tests used to assess the dynamic equations derived here, no special care was taken to either ensure that the tail fin bearings were "cold" or "warm" before the yaw tests were done. Static friction may well have influenced the initial motion of the fins but is unlikely to be important subsequently until it produces a steady-state yaw error. This introduction to bearing friction is provided to record the importance of the difference between static and dynamic friction, and to note the potential need to assess the assumed initial conditions for the modeling of the tail fin yaw behavior.

Static bearing friction was observed as a steady yaw error (at large time) at the lowest $U = 5$ m/s, as shown in Figure 16(b). The error does not occur at higher U, presumably because the aerodynamic loads, which scale as U^2, quickly overcome the static friction. The error is likely to show during starting and stopping of the tail fin at low U but then disappear when the tail fin responds dynamically. This simplifies the modeling because the hysteresis in the moment as tail fin reverses its direction of motion, see (Bonsignore, Ferretti, and Magnani 1999), need not be considered. At $U = 5$ m/s, the steady yaw error was $\gamma_s = 1.35°$. The steady aerodynamic moment, M_s, calculated at this angle is

$$M_s = k_{st}\text{sign}(\gamma_s) = \frac{\pi\rho {b_0}^2}{4}(x_p + \frac{2}{3}c_0)\left(\cos\gamma_s + \frac{K_v}{K_p}|\sin\gamma_s|\right)U^2\sin\gamma_s = 0.0023 \text{ N.m} \tag{9.1}$$

which gives the static friction k_{st}, which we assume to be independent of U.

The dynamic bearing friction for the wind tunnel tests was measured by removing the tail boom, turning the bearing shaft to the horizontal direction, and winding a thin cord supporting a known mass around the shaft. The mass was released and its subsequent motion recorded.

The low-speed bearing frictional torque, Q_f, is dominated by the "rolling frictional moment", (SKF 2023). For application to the tail fin experiments, it is modeled as

$$Q_f \approx \text{sign}(\gamma)k_f|\gamma|^{0.6} \tag{9.2}$$

where the positive "constant" k_f depends on the bearing type, the viscosity of the lubricant, and the axial and radial forces on the bearing. The bearing loads in the friction test differ from those in the wind tunnel experiments, so k_f may well be different, but at least the test results should be compatible with Eqn. (9.2) as demonstrated in Figure 24. To combine the static and dynamic results, the friction is modeled using the exponential model in (Na, Chen, and Ren 2018). The static friction, k_{st}, has two components: the Coulomb friction, k_s, and a "stiction" due to the Stribeck effect as the tail fin accelerates from rest to an angular velocity, n_s, called the Stribeck velocity, with a

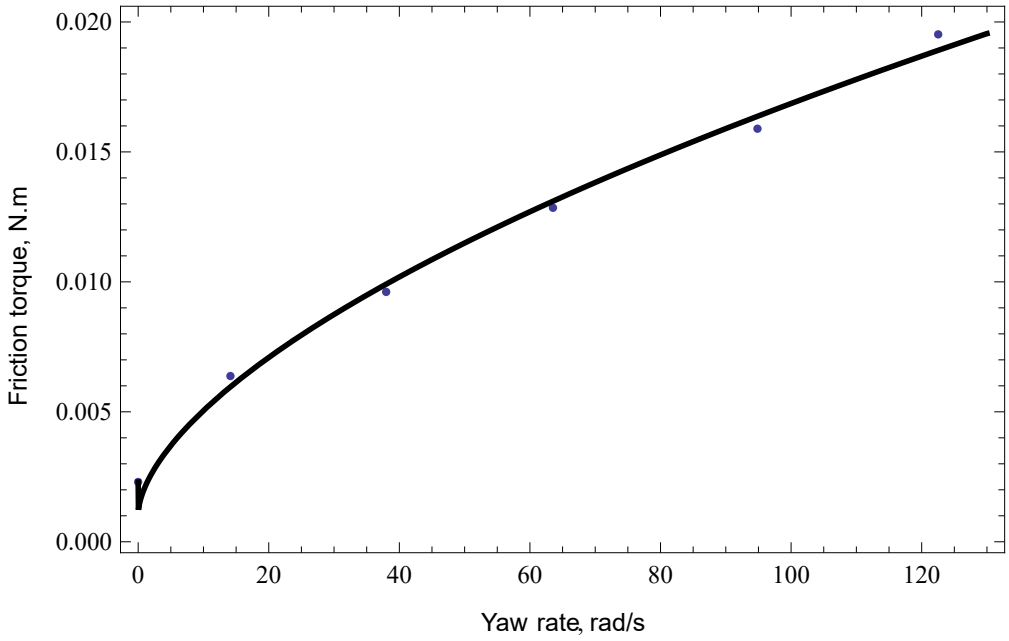

Figure 24. Comparison between the dynamic friction measurements (dots) and Eqn. (9.3) with $k_f = 0.001$ (solid line). The angular velocity on the $x-$axis is treated as the equivalent yaw rate.

friction coefficient, k_d. The frictional torque, Q, acting on the yaw bearing is (Na, Chen, and Ren 2018)

$$Q = \left(k_s + k_d \exp\left[-\left(\frac{\dot{\gamma}}{n_s} \right)^2 \right] + k_f |\gamma|^{0.6} \right) \text{sign}(\gamma) \tag{9.3}$$

where $k_d = k_{st} - k_s$, and k_s is the stiction. The "NonlinearModelFit" function of Mathematica was used to fit the equation to the measured γ after Q was inferred from the steady angular velocity following the release of the masses. This procedure gave the dots shown in Figure 24, with $k_f = 0.001$ N.m/(rad/s)$^{0.6}$, and $k_s = 0.0011$. $n_s = 0.00006$ rad/s was used by (Vaz et al. 2018) and this value was applied in fitting the equation. The combined friction model is shown in Figure 25 for angular velocities more typical of SWT yaw bearings than in Figure 24, which demonstrates the importance of the Stribeck effect. Bearing friction was found to be important only at the lowest $U = 5$ m/s and so was not included in any predictions of the yaw response at $U = 10$ or 17 m/s.

The friction model was included in the aerodynamic model to calculate the response in Figure 16(b) for $U = 5$ m/s, and the results are shown in Figure 26. In principle, the Stribeck effect applies whenever the angular velocity approaches zero as, for example, on approach to the first peak of the response. Whether the static friction model is used in that case or not depends on the value of γ. k_{st} was calculated as described above, based on the angle $\gamma_s = 1.35^\circ$, which is very low. The steady aerodynamic torque will be higher at the higher γ of the first peak. In other words, the friction model is only important when both γ and $\dot{\gamma}$ are small.

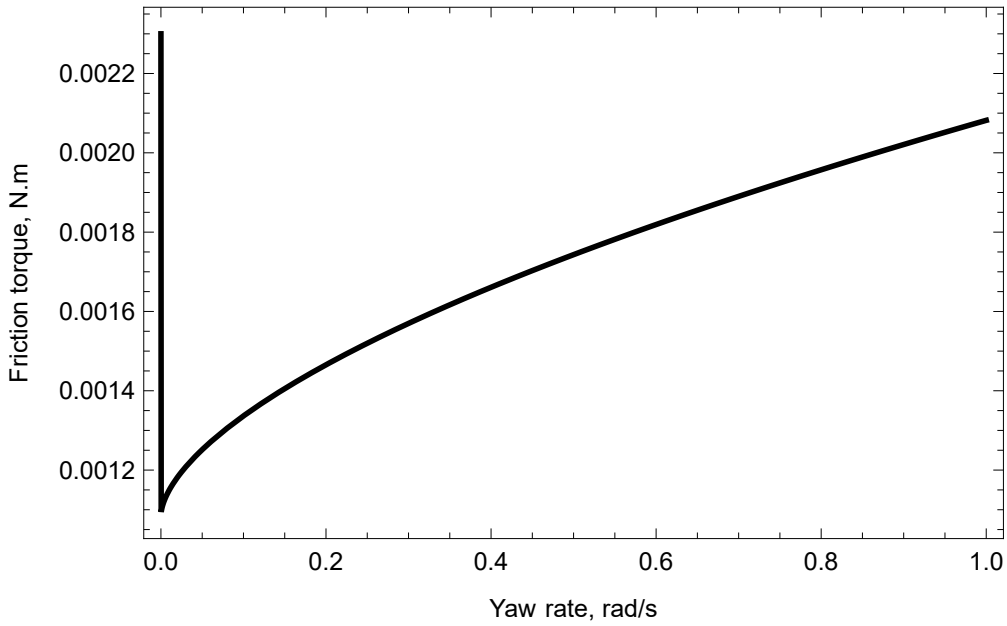

Figure 25. The combined friction model, Eqn. (9.3), demonstrating the importance of the Stribeck effect for yaw rates typical of yawing SWTs. The Stribeck angular velocity $n_s = 0.00006$ rad/s.

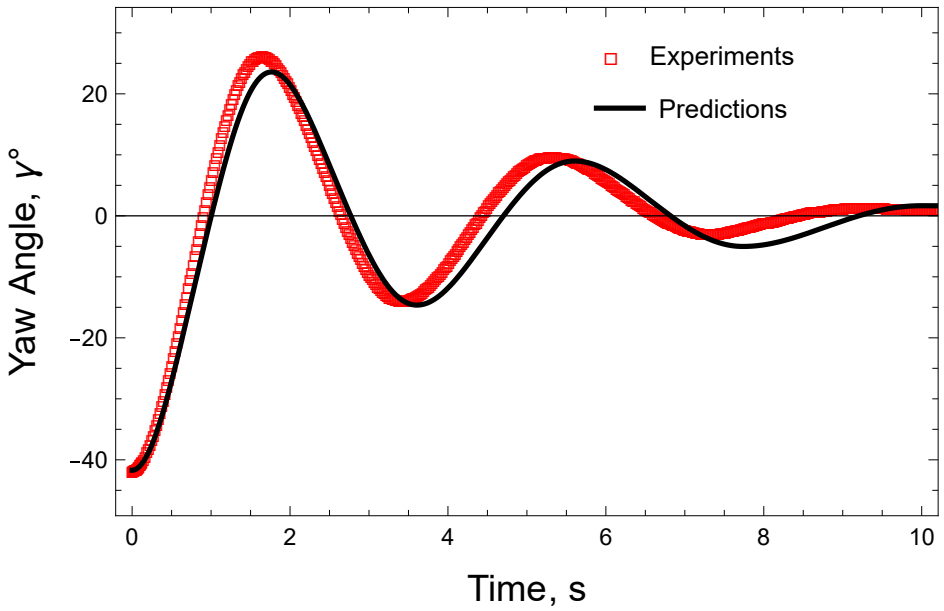

Figure 26. Yaw angle predictions (black line) compared to the experimental results (red □) for a delta wing tail fin of $AR = 0.58, U = 5.0$ m/s and $\gamma_0 = -40°$. The friction model, Eqn. (9.3), is included. Note that $\gamma_s = 1.35°$ was determined from γ at $t = 10$ s.

10 Tail Fin System Identification

The tail fin models developed above contain many parameters. For the generic planforms we have considered, some parameters were extracted from the literature with reasonable certainty, such as the potential flow coefficient, K_p, and vortex lift coefficient, K_v. These coefficients were determined mostly from lifting surface codes for many common planforms as described in Section 11 and represented by simple equations. On the other hand, the parameters involving the separation angles, α^*, and the transition factors, σ, are the least certain considering the range of ARs and planforms. They were simply taken to be the well documented values from delta wing experiments. For that reason, we concentrate on delta fins in this section, but all the important conclusions we draw apply also to elliptical and rectangular fins. System Identification (SI) for the latter is considered in Section 12 in the context of simpler aerodynamic model than the one used here.

It is also possible that a planform selected for a tail fin is not sufficiently close to a documented generic shape to allow easy extrapolation of known parameters. In that case, we recommend simple wind tunnel tests similar to those used here to establish the yaw response. We therefore explored the use of system identification methods to determine the parameters for arbitrary planforms by optimizing the fit of the yaw response equations to the wind tunnel measurements.

Gray box SI was selected to estimate the parameters for any planform by assuming the initial values are those given in Table 2. This should lead to fast convergence and stability in the iterative process of the estimation. This section describes the use of the MATLAB tool box "Nonlinear Grey-Box Models", (Ljung 1995) to estimate the parameters for the planforms tested above. The solution of the model with the initial parameters from Table 2 was compared to the estimated solution using the gray box SI for delta fins at the three wind speeds. In the Matlab code, which is listed in the Appendix, the initial values of all the parameters and their allowable final range are fixed. For all cases, the scaling functions, x_1, x_2, and x_3, are assumed to be given by the static solutions in Eqns. (2.35) and (2.36), because their dynamics would increase the model order significantly without a certain gain in accuracy. Because of the large number of parameters in the present model, several were held fixed during the SI, in particular K_p, K_v, and C_{Dc}.

SI was used first to estimate the parameters at the highest wind speed $U = 17$ m/s and highest $\gamma_0 = -80^\circ$. Then, the process was repeated for the lowest wind speed $U = 5$m/s to show the effect of the friction model on the change of estimated parameters. The estimated parameters at 17 m/s were checked against those at 10 m/s to see the effect of wind speed change on the parameters. Finally, to see the effect of release angle on the parameters, the same process was repeated at $\gamma_0 = -40^\circ$ while keeping the parameters fixed to those at high release angle and $U = 17$ m/s.

The first case is the low $AR = 0.58$ delta tail fin from Section 8.1.1 at 17 m/s and released at -80°, see Figure 17. The parameters $C_{Dc} = 1.3$, $K_p = \pi AR/2$, and $K_v = \pi$ were fixed. The initial values of the other parameters were $\alpha_1^* = 39^\circ$, $\alpha_2^* = \alpha_3^* = 60^\circ$, $\sigma_1 = 0.3$, and $\sigma_2 = \sigma_3 = 0.1$. These were allowed to vary: α_1^* between 30 and 40°. Similarly, $40^\circ \le \alpha_2^* \le 60^\circ$, $60^\circ \le \alpha_3^* \le 80^\circ$, $0 \le \sigma_1 \le 2$, $0 \le \sigma_2 \le 2$, and $0 \le \sigma_3 \le 2$. Also, the friction model was not included for this high wind speed. The predicted yaw angle using the initial parameters is shown in Figure 27(a).[2]. The results are slightly different to those in Figure 17 for which the dynamic equations were used for the x-functions whereas the static approximations were used here. The estimated parameters were $\alpha_1^* = 40^\circ$, $\alpha_2^* = 60^\circ$, $\alpha_3^* = 60^\circ$, $\sigma_1 = 2$, $\sigma_2 = 0.0363$, and $\sigma_3 = 0.0161$. These give an accuracy of the estimated fit of 91%, as shown in Figure 27(b), compared to the calculations using the initial parameters shown in Figure 27(a) with a fit of 70%. The small changes to the α^* values and the larger changes to σ_1, σ_2, and σ_3, which can be seen by comparing Tables 2 and 3, have substantially improved the fit to the data.

For $U = 5$ m/s with the same tail fin released at -80°, the same initial parameters were used together with the friction model from Section 9 with fixed values of $k_s = 0.0011$ N.m, $k_{st} = 0.0023$ N.m, $k_f = 0.001$ N.m/(rad/s)$^{0.6}$, and an initial value of $n_s = 0.00006$ rad/s. The calculated response is shown in Figure 28, for which the estimated parameters were $\alpha_1^* = 40^\circ$, $\alpha_2^* = 60^\circ$, $\alpha_3^* = 60^\circ$, $\sigma_1 = 0.4708$, $\sigma_2 = 0.0381$, and $\sigma_3 = 0.0327$. A value of Stribeck velocity $n_s = 0.4745$ rad/s was estimated. The calculations using the initial parameters in Table 2 gave 86% fit with the data while the estimated parameters, in Table 3, gave 94% as shown in Figure 28 (a) and (b).

[2] As shown in the code listing in the Appendix, the SI outputs were plotted using the Matlab function *compare.m* which is part of the SI toolbox The function does not allow any variation in the plotting, and it was not possible to edit the figure files it produces to make them more consistent with the style of the previous figures.

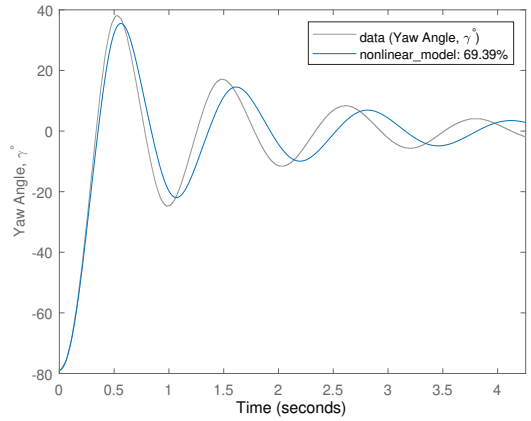

(a) Initial parameter values.

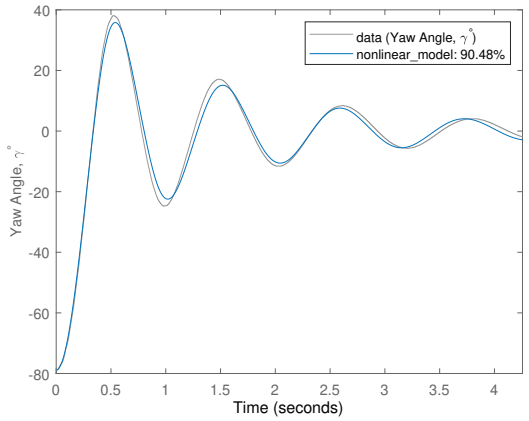

(b) Estimated parameter values.

Figure 27. Calculated (blue line) and measured response (gray line) for the delta tail fin with $AR = 0.58$. $U = 17$ m/s, $\gamma_0 = -80^{\circ}$.

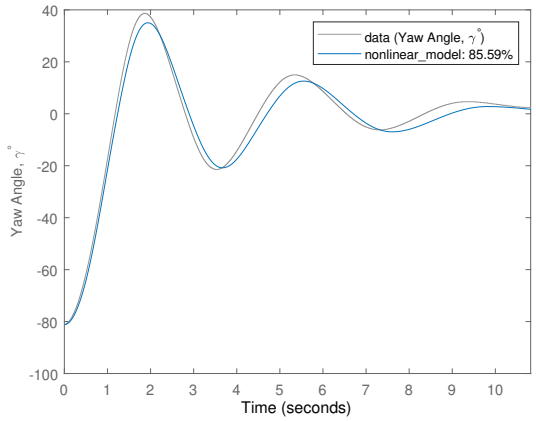

(a) Initial parameter values.

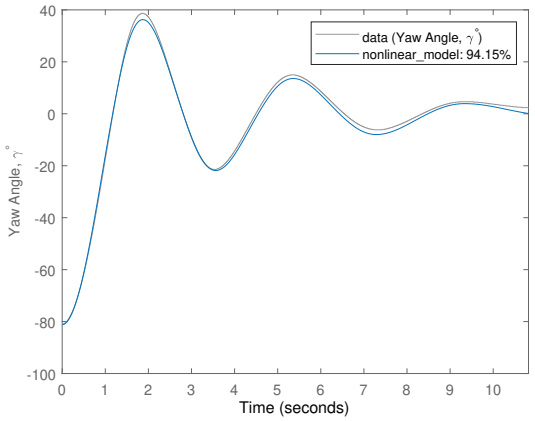

(b) Estimated parameter values.

Figure 28. Calculated (blue line) and measured response (gray line) for the delta tail fin with $AR = 0.58$. $U = 5$ m/s, $\gamma_0 = -80^{\circ}$.

Table 3. Estimated model parameters of a delta tail fin at $\gamma_0 = -80^{\circ}$.

Wind Speed (m/s)	σ_1	σ_2	σ_3	$\alpha_1^*(^{\circ})$	$\alpha_2^*(^{\circ})$	$\alpha_3^*(^{\circ})$
17	2	0.0363	0.0161	40	60	60
5	0.4708	0.0381	0.0327	40	60	60

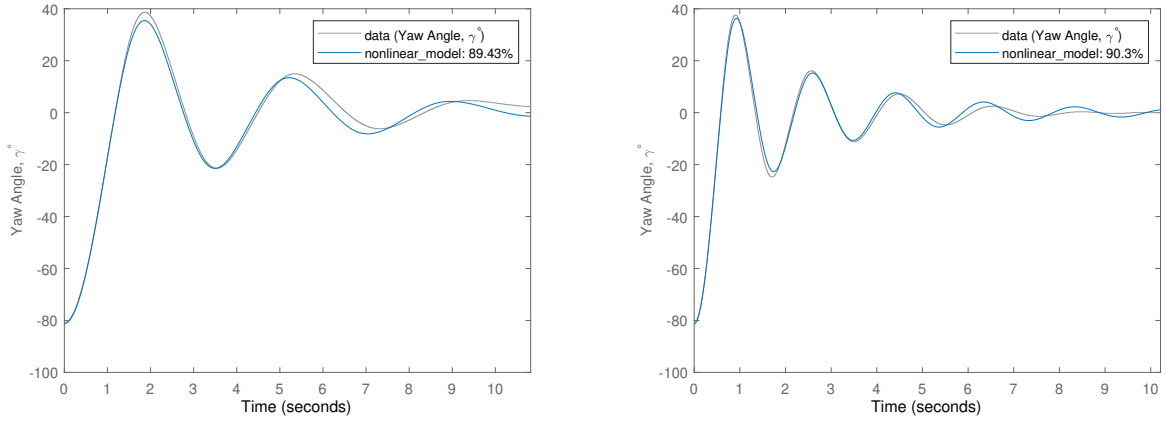

(a) $U = 5$ **m/s using parameters estimated for 17 m/s.** **(b)** $U = 10$ **m/s using parameters estimated for 17 m/s.**

Figure 29. Calculated (blue line) and measured response (gray line) for the delta tail fin with $AR = 0.58$ **and** $\gamma_0 = -80°$**.**

With six parameters to adjust, it is possible that the SI finds local optimal values for each U. On the other hand, the theory developed above has no Reynolds number dependence, so the parameters optimized at any wind speed should apply to any other speed. To test this, the estimated parameters for $U = 17$ m/s were assumed to hold at $U = 5$ m/s, and the response was recalculated as shown in Figure 29(a). The calculated fit is 90%, showing improvement over the initial parameters in Figure 28(a) but not over the estimated response shown in Figure 28(b).

In order to check the effect of U in the absence of friction on the parameters, the values for $U = 17$ m/s were used to calculate the response at 10 m/s where friction can also be disregarded. The response for this case is shown in Figure 29(b). The estimation has a 90% fit which is close to the value in Figure 27(b) for 17 m/s.

Using the estimated parameters from $U = 17$ m/s when the friction model is omitted gives an accuracy of more than 80% at the other wind speeds. What is particularly encouraging is that the initial response, say to the first maximum in $\gamma(t)$, is very accurately identified at all wind speeds. From Figure 15, this is the region where the nonlinear effects are most important. Thus, we recommend that the model parameters be determined by SI at the highest reasonable wind speed where friction is negligible, and high initial yaw angle.

SI has been used to this point only for the $\gamma_0 = -80°$ data. A further check of the generality of the estimated constants was made for $\gamma_0 = -40°$ using the estimated parameters for 17 m/s and $\gamma_0 = -80°$. The fit in Figure 30(a) for 17 m/s was 87% and 84% for 5 m/s in Figure 30(b).

The results of Section 8.3 imply that wind tunnel tests are unlikely to allow meaningful SI for rapidly varying wind speeds. This may not be a major problem, however, as the parameters determining yaw response in unsteady wind are the same as for steady wind.

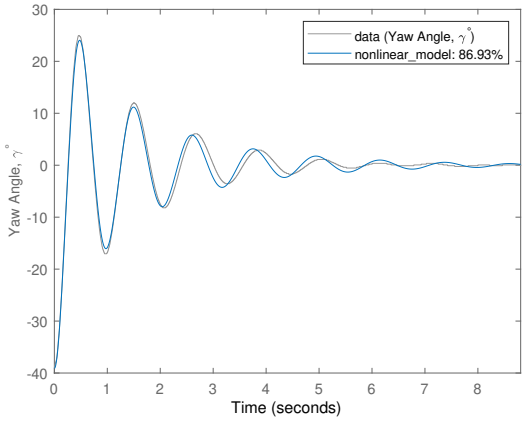

(a) $U = 17$ **m/s using parameters estimated for 17 m/s of Figure 28(b).**

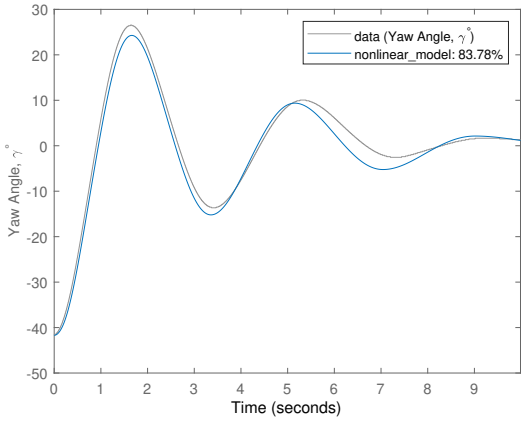

(b) $U = 5$ **m/s using parameters estimated for 17 m/s of Figure 28(b).**

Figure 30. Calculated (blue line) and measured response (gray line) for the delta tail fin with $AR = 0.58$ **and** $\gamma_0 = -40^{\circ}$ **using the estimated parameters for** $\gamma_0 = -80^{\circ}$**.**

11 Characterizing the Yaw Response of a General Planform

We have so far derived the yaw response equations for a limited number of planforms but considered a model for a general tail fin in Section 5. For most tail fins, $c_0/x_p \ll 1$, and W can be assumed constant with x. It is also reasonable to neglect the apparent inertia of the tail fin, which involves $\partial W/\partial t$, compared to the structural moment of inertia, I_z. This assumption was verified by the authors in (Hammam and Wood 2022) and, for example, (Wright 2005) and (Wood 2011). Further, the term containing $\dot{\gamma}^2$ will be significant only at high U and/or high γ. However, even at these conditions, it is likely to be negligible compared to the vortex damping term containing $K_v|\sin\gamma|\dot{\gamma}$. All these considerations mean that the complicated response equations that we have derived may be considerably simplified in many practical cases.

Applying these assumptions and neglecting the effect of vortex breakdown or, equivalently, the three x-functions, the general tail fin dynamic equation, Eqn. (5.2), can be expressed as

$$I_{z,*}\ddot{\gamma} \approx K_p \cos\gamma\left(\frac{\dot{\gamma}r}{U}+\sin\gamma\right)+K_v|\sin\gamma|\left(\frac{2\dot{\gamma}r}{U}+\sin\gamma\right) \tag{11.1}$$

where $I_{z,*} = 2I_z/(\rho A_{tf} U^2 r)$ is the "reduced" inertia and r is the effective length of the tail boom. U is assumed steady, and the rotor effect is neglected, so $W = U\sin\gamma + r\dot{\beta}$. It can be seen from (11.1) that two regimes apply at the two yaw angle limits: potential flow represented by K_p dominates at low γ while vortex flow represented by K_v dominates at high γ. For low γ, Eqn. (11.1) can be approximated as

$$I_{z,*}\ddot{\gamma} \approx K_p\left(\frac{\dot{\gamma}r}{U}+\gamma\right) \tag{11.2}$$

This linear equation is equivalent to that used in prior studies of tail fins, (Bradney, Evans, and Clausen 2018; Singh, Hemmati, and Wood 2012; Wood 2011), and wind vanes, e.g., (Kerhascoët et al. 2016). It also shows that the damping and natural frequency of tail fin motion is mainly a function of K_p and U as demonstrated for the latter by Figure 16(b) even for $|\gamma|$ approaching 40°. Similarly, for high γ the equation reduces to

$$I_{z,*}\ddot{\gamma} \approx K_v\left(\frac{2\dot{\gamma}r}{U}+1\right) \tag{11.3}$$

For the linear (11.3), the time to reach the first peak of the response is called the "peak time" given by

$$T_p = \frac{\pi}{\omega_n\sqrt{1-\zeta^2}} \tag{11.4}$$

where $\omega_n = \sqrt{K_v/I_{z,*}}$ and $\zeta = \sqrt{K_v/I_{z,*}}\,r/(U)$. For $\zeta << 1$, $t_p \approx \pi\sqrt{I_{z,*}/K_v}$ which means that increasing K_v decreases T_p and increases maximum yaw rate of the tail fin. Thus, K_v dictates the value of maximum yaw and has a major effect on the gyroscopic loads on the turbine.

Based on the above discussion, tail fins should have a high K_p in order to respond rapidly at low γ while a reasonable value of K_v to restrain the frequency and the gyroscopic loads on the turbine at very high γ, (Wright and Wood 2007).

The potential flow coefficient K_p or the lift coefficient slope of a slender wings, can be determined based on the planform using the correlation method in (Diederich 1951). K_p for any planform was found to depend only on a function in planform factor F, defined as $F = AR/\cos\Lambda_{c/2}$. This factor is called "equivalent aspect ratio" in (Barnes 2020) that takes the wing sweep into consideration: $\Lambda_{c/2}$ is the sweep of half the chord line. K_p is determined from (Diederich 1951), (Barnes 2020), and (Lowry and Polhamus 1957) as

$$K_p = \frac{2\pi AR}{\sqrt{4+F^2}+2}. \tag{11.5}$$

It can be shown that for low-AR delta wing the relation reduces to $K_p = \pi AR/2$. The half chord sweep for a wing with taper ratio $\lambda = c_t/c_0$ is

$$\tan\Lambda_{c/2} = \tan\Lambda - \frac{2(1-\lambda)}{AR(1+\lambda)} \tag{11.6}$$

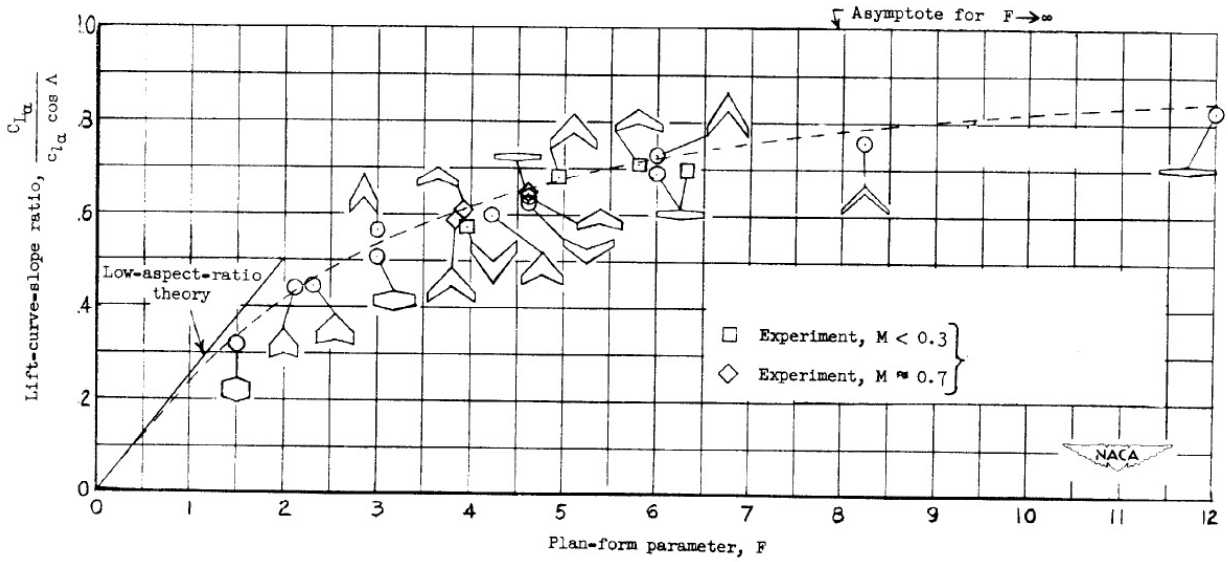

Figure 31. Variation of $K_p/(2\pi\cos\Lambda)$ with F for any planform, (Diederich 1951), $c_{l\alpha} = 2\pi, C_{L\alpha} = K_p$.

where c_t is the tip chord of a tapered wing, (Lowry and Polhamus 1957). Using Eqns. (11.5) condenses the calculation of K_p for any planform as shown in Figure 31.

An example application of the above relations for a delta wing of $\Lambda = 80°$ can be checked against the value of K_p in Eqn. (4.5). For this planform, $AR = 4/\tan\Lambda = 0.71$. This gives $K_p = 0.98$ from Eqn. (4.5). For the application of the current method, $\Lambda_{c/2} = 70.7°$ from Eqn. (11.6). This gives $F = 2.15$; hence, from Eqn. (11.5), $K_p = 0.91$, which is within 10% of the value calculated from Eqn. (4.5).

The second important parameter is the vortex force coefficient, K_v, which dominates the tail fin response at high γ. As K_v results from flow separation from all the sharp edges of a tail fin except the trailing edge, it has multiple contributions as noted above for rectangular fins, and as discussed in (Lamar 1974). For example, a cropped wing with swept leading-edges gives rise to $K_{v,le}$ and side edges to $K_{v,se}$. In addition, it was shown in Section 6 that an augmented vortex force arises due to the sustained effect of the LEV aft of maximum width as shown in Figure 10. According to (Lamar 1974), K_v for a general tail fin is given from

$$K_v = K_{v,le} + K_{v,se} + K_{v,a} \tag{11.7}$$

where $K_{v,a}$ is the augmented vortex lift coefficient introduced in Section 6. As K_v is responsible for the frequency of tail fin motion at high γ, it should be controlled to minimize the gyroscopic loads as mentioned above. This could be taken into account by controlling the three vortex force components through the choice of planform.

Another important case of tail fin operation as stated in Section 3.1 is in reverse flow when $]\gamma| > 90°$. For asymmetric (in the x-direction) tail fins such as a delta wing, this causes a loss in $K_{v,le}$ because the leading-edge becomes unswept in reverse flow, which could reduce the ability to orient the turbine to the wind at high γ. It was shown in Section 3.1 that the potential flow for a reverse tail fin is close to that for the regular one; however, the large decrease in $K_{v,le}$ could reduce the important contribution of the vortex flow on the tail fin dynamics in reverse flow. At the same time, $K_{v,se}$ will act in forward and reverse flow in the same way, so having a tail fin with a reasonable value of $K_{v,se}$ is likely to be crucial for effective operation of the tail fin in reverse flow.

A tail fin, therefore, should have a high K_p, reasonable K_v, and high $K_{v,se}$. It will be shown in the following that increasing K_p increases $K_{v,le}$, so a way of increasing K_p without having very high K_v is to have a negative $K_{v,a}$. Another important aspect is that to increase K_p requires a large AR. One main method of increasing AR is through reduction in tail fin sweep Λ, but this will cause the LEV to break down at a small angle of attack (Figure 4). This reduces the performance of the tail fin significantly at high γ. To increase AR for constant Λ, the trailing edge can be positively notched; the notch length is the streamwise distance measured from the tip to the trailing edge at $y =$

0. Notching the trailing edge results in an arrow planform. Before expanding on these arguments, a method of calculating the different components of the vortex force is explained in the next section.

11.1 Determining the Vortex Force Coefficients

We now consider the determination of the three components of K_v in Eqn. (11.7) for planforms that are modifications of the generic delta wing. The LEV coefficient can be determined directly from the K_p and Λ of a tail fin. (Polhamus 1966) shows the suction analogy gives the relation between $K_{v,le}$ and K_p as

$$K_{v,le} = K_p(1 - K_p K_i)/\cos\Lambda \tag{11.8}$$

where $K_i = \partial C_{D,i}/\partial C_L^2$. C_L is the tail fin lift coefficient and $C_{D,i} = C_L^2/(\pi AR)$ is the induced drag coefficient, (Traub 1997). So, $K_i = 1/(\pi AR)$. For the delta wing example above $\Lambda = 80^\circ$, $K_p = 0.98$, and $AR = 0.71$, so $K_v = K_{v,le} = 3.16 \approx \pi$.

The augmented $K_{v,a}$ is due to the LEV traversing the surface aft of the maximum b. From (Lamar 1976b)

$$K_{v,a} = 2K_{v,le}\cos\Lambda c^*/b_0 \tag{11.9}$$

where the term multiplying c^* resembles $K_{v,le}$ averaged over the span b_0 and c^* is a characteristic chord length that is determined empirically in (Lamar 1976b) to be the streamwise distance from points B to points D in Figure 32. c^* could have negative value as in the arrow delta wing planform, (Lamar 1976b). In this case this component of vortex force contributes negatively to K_v which could be an advantage in limiting the value of K_v.

The side edge vortex coefficient $K_{v,se}$ increases with increasing Λ and λ, but decreases with AR, (Lamar 1976a). A good correlation of $K_{v,se}$ with these parameters is found from the lifting surface theory results in (Lamar 1976b):

$$K_{v,se} = \frac{4\pi\lambda}{(1+\lambda)(AR+2)\sqrt[7]{\cos\Lambda}} \tag{11.10}$$

which reduces to Eqn. (7.4) for a rectangular wing with $\Lambda = 0^\circ$ and $\lambda = 1$. It also reduces to the common result that at $AR = 0$, $K_{v_{se}} = \pi$, (Lamar 1974). Eqns. (11.5), (11.8), (11.9), and (11.10) were checked against some planforms with known coefficients from lifting surface theories in (Lamar and Gloss 1975). For the planforms in Figure 32, the comparison is given in Table 4. It is important to note that all three components of K_v have similar magnitudes. Table 4 shows that the predicted coefficients compare well to the ones listed in (Lamar 1976b).

Table 4. Comparison between force coefficients calculated and those from (Lamar 1976b) for various planforms with $\Lambda = 63^\circ$ shown in Figure 32. Numbers in parentheses are equations in this report.

Tail fin planform	K_p	K_p (11.5)	$K_{v,le}$	$K_{v,le}$ (11.8)	$K_{v,se}$	$K_{v,se}$ (11.10)	$K_{v,a}$	$K_{v,a}$ (11.9)
Cropped delta ($AR = 0.873, \lambda = 0.4$)	1.279	1.26	1.504	1.5	1.397	1.3	0.893	0.891
Cropped arrow ($AR = 1.069, \lambda = 0.538$)	1.487	1.42	1.824	1.81	1.693	1.43	0.389	0.382
Cropped diamond ($AR = 0.738, \lambda = 0.318$)	1.107	1.11	1.274	1.27	1.2	1.19	1.242	1.24

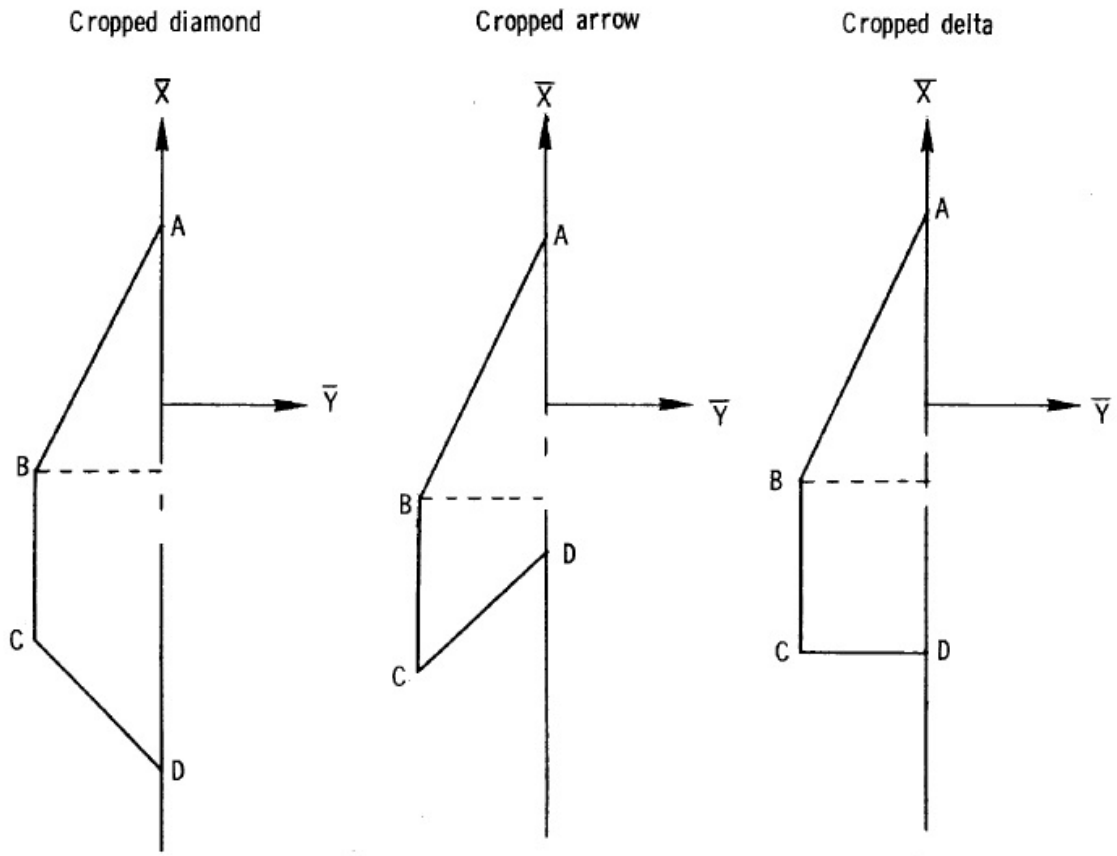

Point	$\bar{x}$	$\bar{y}$
A	1.54985	0.0
B	-0.41276	-1.0
C	-1.72117	-1.0
D	-2.56025	0.0

Point	$\bar{x}$	$\bar{y}$
A	1.36465	0.0
B	-0.59796	-1.0
C	-1.90637	-1.0
D	-1.06725	0.0

Point	$\bar{x}$	$\bar{y}$
A	1.44858	0.0
B	-0.51403	-1.0
C	-1.8224	-1.0
D	-1.8224	0.0

Figure 32. Different cropped planforms, (Lamar and Gloss 1975). All dimensions are in cm.

12 Tail fin Planform Assessment

The planform has a major effect on the yaw response as shown, for example, by Eqn. (11.1). Tail fins need a high K_p for good response at low γ without a large K_v to minimize the yaw rate at high γ. In addition, a high Λ will avoid vortex breakdown at low α, or low γ. One last requirement is to have a reasonable value of $K_{v,se}$ in order to have sufficient moment to reorient the turbine downwind if very high yaw angles are encountered during starting at low wind speed.

To increase K_p without reducing Λ, the tail fin could be "notched." Notching can be thought of as removing a delta wing of the same b_0 but higher AR from the trailing edge to leave it having a delta shape similar to the leading-edge. The first planform in Figure 32 is negatively notched, and the middle one is positively notched to give a cropped arrow. The notch ratio, a/b_0, where a is the x-distance from point D to C, should be sufficiently positive to provide high AR and negative augmented vortex lift $K_{v,a}$. This tends to not increase K_v too much as a result of increasing AR. At the same time it should have a reasonable taper ratio, $\lambda = BC/AD$, to achieve a reasonable $K_{v,se}$. The three tapered planforms in Figure 32 are characterised by their different λ, which are listed in Table 4 along with their vortex force coefficients in the second and subsequent columns. A reasonable value of $K_{v,se}$ helps to orient the tail fin upwind at low wind speed from a high γ_0.

A further required feature of this tail fin is to increase its sweep angle given by

$$\tan\Lambda = \frac{4(1-\lambda)}{AR(1+\lambda)} + \frac{2a}{b_0} \tag{12.1}$$

One way of increasing Λ without affecting the aspect ratio is to have $\lambda = 1$. However, increasing Λ to very high values could make K_p independent of AR, as can be seen from Eqn. (11.5): as Λ increases, $K_p \to 2\pi\cos\Lambda$, which becomes low. Thus, Λ should be moderate for notched planforms, which may deteriorate the performance due to vortex breakdown at low angle of attack.

Another more obvious way of having similar performance for the upwind and downwind orientation is to have a rectangular tail fin. This tail fin would have similar K_p as a delta wing of the same AR, but it would have high $K_{v,se}$ that would assist the turbine starting with large yaw. A possible problem with rectangular tail fins is that the center of pressure is at the leading-edge theoretically and very close to it actually. This will reduce the yaw moment arm, but only slightly if $c_0/x_p \ll 1$. Even though rectangular tail fins have the limiting value of $\Lambda = 0°$, their stall characteristics in terms of vortex breakdown and maximum lift have been shown experimentally to be similar to those of delta wings of the same AR, (Lamar 1974; DeVoria and Mohseni 2017; Bollay 1937).

13 The Reduced Equation for Tail Fins

13.1 Analytical Response

In this section, the reduced Eqn. (11.1) and two simple extensions of it, are compared to the full models of Section 5 for the three generic planforms. We start with the comparison of Eqn. (11.1) in Figure 33(a) for a delta fin, when $r = x_p$ is assumed. It can be seen that both frequency and damping are underpredicted. Since the restriction $c_0/x_p \ll 1$, required to derive Eqn. (11.1), is not satisfied, the model was recalculated assuming $r = x_p + 2/3c_0$, which predicts a marginally higher damping term while slightly underpredicting the response frequency (Figure 33(b)).

To check their significance, the flow functions x_i defined in Section 2.1.1, were added to Eqn. (11.1) to give

$$I_{z,*}\ddot{\gamma} = x_1 K_p \left(\frac{\dot{\gamma} r}{U} + \sin\gamma\right)\cos\gamma + \left(x_2 K_v |\sin\gamma| + (1-x_3)C_{Dc}\right)\left(\frac{2\dot{\gamma} r}{U} + \sin\gamma\right) \tag{13.1}$$

where x_i are taken from Eqn. (2.34), and $C_{Dc} = 1.3$. Introducing $r_1 = x_p + f_1 c_0$ and $r_2 = x_p + f_2 c_0$ to separate the damping moment arm and steady-state moment arm, where $0 \le f_1, f_2 \le 1$ depending on the planform, the model becomes

$$I_{z,*}\ddot{\gamma} = x_1 K_p \left(\frac{\dot{\gamma} r_1^2}{U r} + \frac{r_2}{r}\sin\gamma\right)\cos\gamma + \left(x_2 K_v |\sin\gamma| + (1-x_3)C_{Dc}\right)\left(\frac{2\dot{\gamma} r_1^2}{U r} + \frac{r_2}{r}\sin\gamma\right) \tag{13.2}$$

In order to check the effect of planform on its accuracy, the reduced model, Eqn. (13.2), is compared to the full model, Eqn. (8.4), for the elliptical fin at low $AR = 0.37$ in Figure 34(a). In this case the reduced equation's damping is lower than the measurements due to assuming the damping moment arm the same as the center of pressure $r = r_1 = r_2 = x_p + c_0/6$.

For the rectangular tail fin with $r_1 = x_p + c_0$ and $r_2 = x_p$, the prediction for $AR = 0.5$ is shown in Figure 34(b). The reduced model predicts lower frequency than the measurements and the full model of Eqn. (8.6). Increasing r_2 according to Eqn.(7.2) is expected to improve the predictions of the reduced model.

It can be concluded that the reduced model is a promising alternative to the complicated full models, if the appropriate moment arms and force coefficients of the different planforms are used. When these parameters are known or have been determined experimentally, the response of tail fins of any planforms can be calculated simply and with good accuracy using the reduced model. It must be remembered, however, that the reduced model predicts lower damping than in the measurements because it neglects the $\dot{\gamma}^2$ term, but this effect was shown to be small.

13.2 System Identification of the Reduced Equation

In Section 10, SI was used to increase the accuracy of the fit of the full model by adjusting the less-well-known aerodynamic parameters of the generic delta planform while keeping C_{Dc}, K_p, and K_v fixed. SI may, however, become computationally intensive or unstable if it was used to estimate the force coefficients K_p, and K_v for general planforms. The reduced model, however, could be a reasonable alternative since it contains fewer parameters.

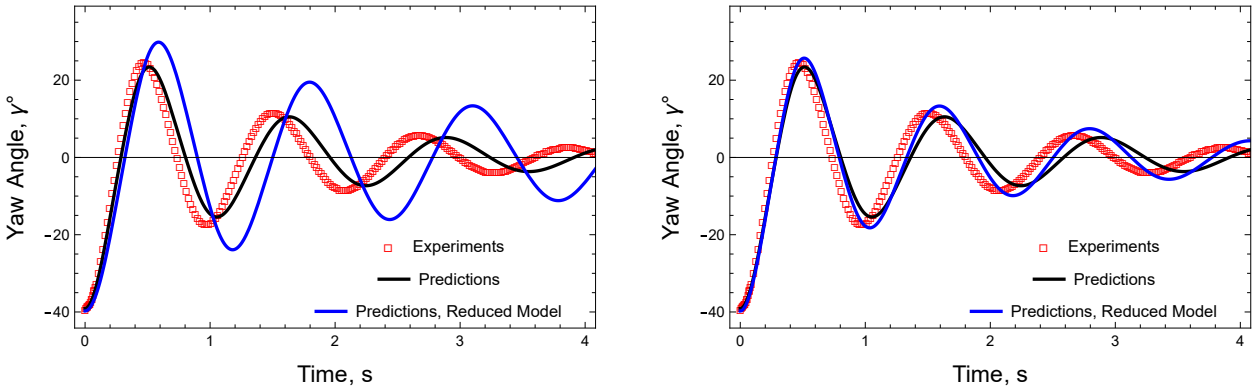

(a) $r = x_p$. **(b)** $r = x_p + c_0$.

Figure 33. Yaw angle predictions of the delta fin using full Eqn. (8.2) (black line) and reduced model Eqn. (11.1) (blue line), and the experimental results (red □). $AR = 0.58$, $U = 17$ **m/s,** $\gamma_0 = -40°$.

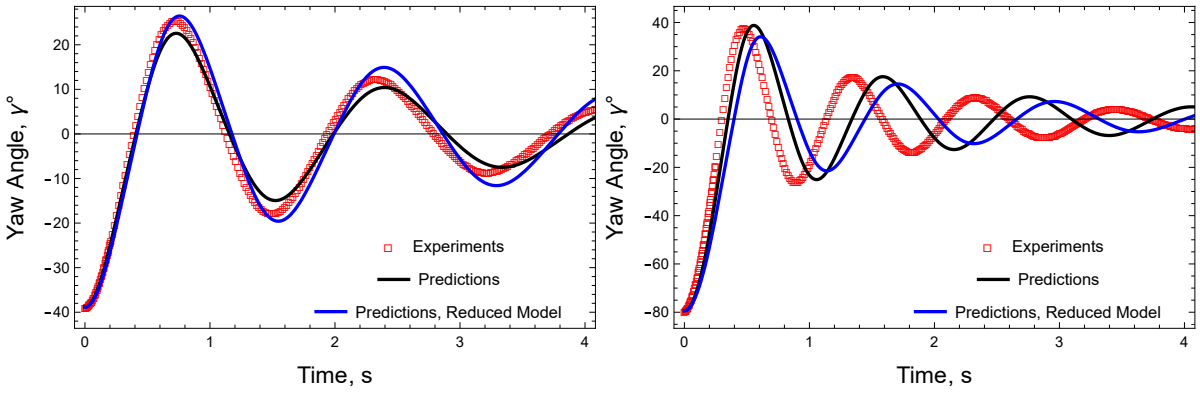

(a) Elliptical fin, $AR = 0.37, U = 10$ m/s, $\gamma_0 = -40°$, and $r = r_1 = r_2 = x_p + c_0/6$.

(b) Rectangular fin, $AR = 0.5, U = 17$m/s, $\gamma_0 = -80°$, $r = r_1 = x_p + c_0$, and $r_2 = x_p$.

Figure 34. Yaw angle predictions of a) the elliptical fin using full Eqn. (8.4) (black line), reduced model Eqn. (13.2) (blue line), and the experimental results (red □), b) the rectangular fin using the full model Eqn. (8.6) (black line), reduced model Eqn. (13.2) (blue line), and the experimental results (red □).

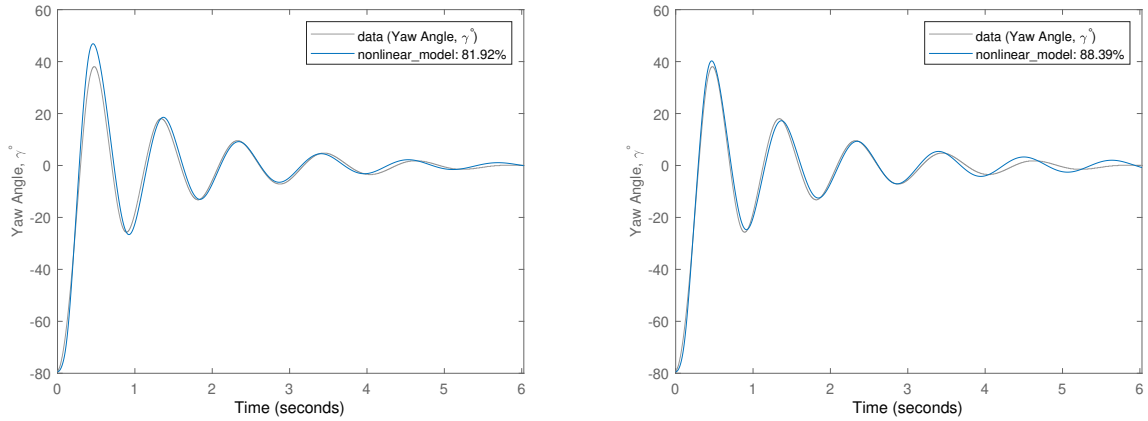

(a) Reduced Eqn. (13.2).

(b) Full Eqn.(8.6)

Figure 35. Yaw angle estimation of the rectangular wing fin using reduced model Eqn. (13.2) in (a) and full model Eqn. (8.6) in (b) compared to the experimental results in blue line . $AR = 0.5, U = 17$ m/s, $\gamma_0 = -80°$, and $r_1 = x_p + c_0$.

A good test case for SI with the reduced model is the rectangular tail fin, which showed the least accurate prediction of the full model in Figure 19. In this test the values of K_p, K_v , C_{Dc}, σ_1, σ_2, σ_3, and α_1^*, α_2^*, α_3^*, and r_2 were estimated. The estimated response using the reduced model is shown in Figure 35 for the rectangular tail fin of $AR = 0.5$. The estimated parameters are $K_p = 1.3$, $K_v = 3.56$, $C_{Dc} = 1.46$, $\sigma_1 = 0.49$, $\sigma_2 = 0.17$, $\sigma_3 = 0.045$, and $\alpha_1^* = 39.7°$, $\alpha_2^* = 60°$, $\alpha_3^* = 60°$, and $r_2 = x_p + c_0/8$. The fit of the estimation was 82%, due mainly to the higher estimated damping.

To compare the effectiveness of SI with the full model, the same case was investigated using Eqn. (8.6), and the estimation is shown in Figure 35(b). The aerodynamic synthesising parameters α_i^* and σ_i were left free while the other parameters were fixed as was done in Section 10. The estimated parameters are $\sigma_1 = 0.1815$, $\sigma_2 = 0.1175$, $\sigma_3 = 0.0101$, and $\alpha_1^* = 40°$, $\alpha_2^* = 60°$, $\alpha_3^* = 60°$. The fit is 89%, which is not only better than the reduced model but the values of K_p and K_v are kept the same to those in Table 2.

In summary: even though the reduced model, or Eqn.(13.2), predicts the response to a similar accuracy as the full model, the parameters used in the reduced model should be estimated by system identification using the full model.

13.3 Reduced Model for OpenFAST

The general aerodynamic equations of tail fin yaw are given in Section 5. These equations are valid under general conditions without restricting assumptions. They are also essential for estimating accurate values of the model parameters as shown in Section 13.2. Under practical conditions, however, tail fins usually satisfy the condition $c_0 \ll x_p$, which means that the velocities acting on the tail fin do not change over the chord, and x_p can be considered the reference length in the moment equation. This resulted in the reduced model of Eqn. (13.2).

The reduced model gives the tail fin response in terms of parameters K_p, K_v, C_{Dc}, and the x-functions, and the moment arm. In this section the reduced model will be extended to include the effect of V_{el} and V_{in} velocity components as defined in Figure 1. From Eqn.(5.1), the normal force acting on the tail fin assuming W is constant in time and length, is

$$N = -\frac{\pi\rho}{4}x_1 V_x W \int_{x_p}^{x_p+c_0}(1 - \frac{x-x_p}{c_0}\sin\varepsilon)\frac{\partial b(x)^2}{\partial x}dx - \frac{\rho}{2}W^2\Big[x_2K_v + (1 - x_3)C_{Dc}\Big]\int_{x_p}^{x_p+c_0} b(x)dx. \quad (13.3)$$

The last integral of $b(x)$ is just A_{tf}, and the first can be rewritten in terms of the high-AR form of K_p, to give

$$N = -\frac{\rho}{2}A_{tf}K_p x_1 V_x W - \frac{\rho}{2}A_{tf}\Big[x_2K_v + (1-x_3)C_{Dc}\Big]W^2. \quad (13.4)$$

K_p can be determined for the generic shape by, for example, Eqn. (4.5) for the delta tail fin, or approximated by Eqn. (11.5). Similarly, the moment equation at the apex (5.2) for the same conditions is

$$M_a = -\frac{\pi\rho}{4}x_1 V_x W \int_{x_p}^{x_p+c_0}\left(1 - \frac{x-x_p}{c_0}\sin\varepsilon\right)\frac{\partial b^2(x)}{\partial x}(x-x_p)dx - \frac{\rho}{2}\Big[x_2K_v + (1-x_3)C_{Dc}\Big]W^2\int_{x_p}^{x_p+c_0} b(x)(x-x_p)dx. \quad (13.5)$$

For the wind tunnel tests in Section 13, c_0 was not small compared to x_p, which caused x_{cp} to vary with c_0. For many SWTs, however, $c_0 \ll x_p$, and so $x_{cp} \approx x_p$. Eqn. (13.5) can then be solved to give

$$M_a = -\frac{\rho}{2}A_{tf}x_{cp}x_1K_pV_xW - \frac{\rho}{2}A_{tf}x_{cp}\Big[x_2K_v + (1-x_3)C_{Dc}\Big]W^2. \quad (13.6)$$

The advantage of these formulation is that they give the force and moment in analytic form in terms of parameters that are AR and planform-dependent. For example, K_p and K_v could be determined for different planforms from Section 11.

14 The Current Model Compared to the Polar Model from OpenFAST v3.4

Since this work was motivated primarily by the need to develop a new tail fin model for OpenFAST, it is appropriate to comment on its relation to the tail fin model used in OpenFAST v3.4, the last release that had a tail fin model. This is a "polar model" relying on a lookup table of tail fin lift and drag. Even though the model can accommodate nonlinear forces, it has some shortcomings. First it assumes a fixed center of pressure in the tail fin moment equation, which is valid only for $c_0 \ll x_p$ as shown in Section 13. Secondly, it assumes that lift and drag are the resultant forces acting on tail fin surface; however, as shown in Section 2.1.1 for sharp-edged tail fin, the force normal to the chord of the tail fin is the only cause of yaw moment. As explained in Section 2.1.2, the LEV orients the force normally to the tail fin as shown in Figure 3. In addition, the associated thrust cancels the force of the potential flow in the tangential direction. In other words, the effect of induced drag of the tail fin is diminished. Finally, the polar model is a quasi-steady one and so ignores the terms in the moment equation that depend on the yaw rate and acceleration, which are obvious in, for example, Eqn. (8.2).

Moreover, the current model allows synthesizing the normal force coefficients for most tail fin planforms for any aspect ratio, sweep angle, taper, and notch ratios for a wide range of $\alpha < |180°|$. This analytic representation is more general than the lookup table in the OpenFAST v3.4 model, which is likely to be hard to construct except for some simple planforms at low aspect ratios.

For unusual planforms not covered in the current report, SI of wind tunnel test results allows systematic identification of the parameters describing the tail fin aerodynamics.

15 Summary, Conclusions, and Recommendations

This report develops nonlinear equations for the yaw response of a tail fin for small wind turbines in a manner that can be implemented in the NREL aeroelastic code OpenFAST.

The linear theory of tail fins and wind vanes is well understood and has some important consequences, (Bradney, Evans, and Clausen 2018; Singh, Hemmati, and Wood 2012; Wood 2011; Kerhascoët et al. 2016). For example, it is easy to show on dimensional grounds that in the absence of Reynolds number effects, the frequency of the yaw response is proportional to the wind speed at the tail fin. An extension to the nonlinear regime, however, is needed for two main reasons. The first is to account for high angles of attack and the second is to generalize the tail fin model beyond the generic shapes of delta wings, rectangles, and ellipses for which the linearized equations are known for low aspect ratios. We assume that higher aspect ratio and more complex planforms retain the simplification that Reynolds number effects are small. Even for the generic shapes, high aspect ratio can seriously complicate the linear unsteady slender body theory (USBT) that is the basis of tail fin analysis described herein. In addition, we argue that high angles of attack occur most often during the starting of small wind turbines at low wind speed where the friction in the yaw bearing assembly may well influence the yaw behavior. Thus a friction model was developed by accounting for the well-known difference between static and dynamic friction and using additional inputs from measurements of yaw bearing friction.

Our approach was to extend USBT to high angles and aspect ratios and test the resulting formulations against wind tunnel experiments of tail fin yaw response in the absence of a nacelle and rotor. The experiments confirmed the wind speed dependence of the response frequency. Unsurprisingly, the low-angle response is dominated by the "potential flow coefficient" K_p, which gives way to the "vortex coefficient" K_v at high angles. The implementation of K_v follows the analysis of (Polhamus 1966) who quantified the increase in delta wing lift due to vortices shed from the leading and side edges at high angles. Additional unsteady effects such as vortex bursting or breakdown, are modeled in the literature and herein by simple linear differential equations.

Our nonlinear equations for the generic shapes at high angles and aspect ratios generally gave good predictions of the wind tunnel experiments, but the complete equations are complicated and contain parameters whose values are not well established. Thus we used system identification (SI) techniques to optimize the fit of the equations to the wind tunnel measurements; small adjustments to the parameters led to significant improvements in the accuracy of fitting the model to the data. Also, it is generally sufficient to identify three model parameters that express the relative importance of the different flow components with angle of attack.

The complexity of the complete equations suggested the need for reduced forms, so Eqn. (11.1) and its variations were developed through a careful assessment of the relative importance of the terms in the complete equations. The reduced equations gave similar accuracy as the full equations, if the appropriate values of different parameters are used, and are easier to deal with. We conclude that USBT provides a good framework to develop tail fin models and to understand the desirable features of them. For example, we argue that a tail fin requires a high K_p to track the wind at low angles and only a moderate K_v to avoid excessive yaw rates at high angles. In addition, the reverse flow over tail fins was considered on the grounds that they may experience very high angles of yaw.

The full model of tail fin yaw response allows for more accurate SI than the reduced model as shown in Section 13.2: the full model produced a fit to the measured response of over 80% in most cases. This high accuracy for a nonlinear second-order model is considered a powerful result in describing the tail fin yaw response. Also, the full model was shown to achieve a better fit than the reduced model by allowing only a small number of adjustable parameters. Part of the strength of the full model is that the moment arms of the different force components are separately modeled and identified. This is compared to the reduced model, which assumes the moment arm of the damping term, with the center of pressure assumed to be the same for both potential and vortex flow models, whereas they can differ in the full model. The full model accommodates a varying velocity distribution over the tail fin, which becomes important when the chord is not small compared to the tail boom length, which applies to the tail fin models used in the wind tunnel tests, Section 8. The full model allowed the ranges for these parameters to be specified in the SI, which probably helped to stabilize the process.

Based on the above, we conclude that the full model of Section 5 should be used for tail fin parameter estimation when the planform is similar to the generic shapes considered here. Only the dependence of the flow functions x_i for $i = \{1,2,3\}$ on the transition angles α_i^* and decay rates σ_i should be estimated, by fitting the model to the results of

wind tunnel experiments similar to those described here. Also, the report provides equations for the force coefficients K_p and K_v for planforms of any taper, sweep angle, notch ratio and aspect ratio. For planforms that differ significantly from the ones described by these shape parameters, the coefficients and the moment arms should be estimated from wind tunnel tests using an SI code similar to that in the Appendix. The estimation process should specify a range for the parameters to be estimated based on the physical constraints stated in the report in order to avoid unphysical values. The SI should be performed at the highest tunnel speed and tail fin release angle possible using the full model. The optimized parameters should apply at other wind speeds and release angles with a reasonable accuracy.

The reduced model, Eqns. (13.4) and (13.6), can be used with a good accuracy when the tail fin satisfies the condition $c_0/x_p \ll 1$. Finally, it is important to note that a major limitation of the wind tunnel tests was their inability to produce a time variation in the wind speed that was sufficiently large to test the USBT equations. Despite the time-dependent terms containing only parameters that govern the steady wind speed response, it is likely that field measurements of SWT yaw will be needed to fully assess the theory.

References

Amiet, R. K. 1995. "Airfoil leading-edge suction and energy conservation for compressible flow." *Journal of Fluid Mechanics* 289:227–242.

Barnes, J., and J. Barnes. 1997. "Semi-empirical vortex step method for the lift and induced drag loading of 2D or 3D wings." In *1997 World Aviation Congress,* 5559.

Barnes, J. P. 2020. "Configuration aerodynamics-classical methods applied." In *AIAA Aviation 2020 Forum,* 2708.

Bollay, W. 1937. "A theory for rectangular wings of small aspect ratio." *Journal of the Aeronautical Sciences* 4 (7): 294–296.

Bonsignore, A., G. Ferretti, and G. Magnani. 1999. "Analytical formulation of the classical friction model for motion analysis and simulation." *Mathematical and Computer Modelling of Dynamical Systems* 5 (1): 43–54.

Bradney, D., S. Evans, and P. Clausen. 2018. "The Effect of Tail Fin Size on the Yaw Performance of Small Wind Turbines Operating in Unsteady Flow." In *Colloquium on Research and Innovation on Wind Energy on Exploitation in Urban Environment Colloquium,* 55–70. Springer.

Brown, C. E. 1946. *Theoretical lift and drag of thin triangular wings at supersonic speeds.* Technical report. NACA-TR-839.

Cohen, D., and R. T. Jones. 2015. *High speed wing theory.* Vol. 2204. Princeton University Press.

DeVoria, A. C., and K. Mohseni. 2017. "A vortex model for forces and moments on low-aspect-ratio wings in side-slip with experimental validation." *Proceedings of the Royal Society A: Mathematical, Physical and Engineering Sciences* 473 (2198): 20160760.

Diederich, F. W. 1951. *A plan-form parameter for correlating certain aerodynamic characteristics of swept wings.* Technical report. NACA-TN-2335.

Dore, B. D. 1966. "Non-linear theory for slender wings in sudden plunging motion." *Aeronautical Quarterly* 17 (2): 187–200.

Evans, S., S. Dana, P. Clausen, and D. Wood. 2021. "A simple method for modelling fatigue spectra of small wind turbine blades." *Wind Energy* 24 (6): 549–557.

Fan, Y., and F. Lutze. 1996. "Identification of an unsteady aerodynamic model at high angles of attack." In *21st Atmospheric Flight Mechanics Conference,* 3407.

Gibson, B., and H. Gerhardt. 1993. "Development of an innovative natural laminar flow wing concept for high-speed civil transports." In *11th Applied Aerodynamics Conference,* 3466.

Goman, M., and A. Khrabrov. 1994. "State-space representation of aerodynamic characteristics of an aircraft at high angles of attack." *Journal of Aircraft* 31 (5): 1109–1115.

Hammam, M. M., and D. H. Wood. 2022. "Aeroelastic modelling of tail fins for small wind turbines." *Journal of Physics: Conference Series* 2265 (4): 042073.

Hauptman, A., and T. Miloh. 1986. "On the exact solution of the linearized lifting-surface problem of an elliptic wing." *The Quarterly Journal of Mechanics and Applied Mathematics* 39 (1): 41–66.

Helmbold, H. B. 1942. *Der unvurwundene ellipsenfliigel als tragende fliiche. Report, der Deutschen Luftfahrt-forschung.*

Hopkins, E. J. 1951. *Lift, pitching moment, and span load characteristics of wings at low speed as affected by variations of sweep and aspect ratio.* Technical report 2284. NACA TN-2284.

IEC. 2013. *IEC 61400–2: Wind turbines—part 2: small wind turbines.*

Jarrah, M.-A. M. 1989. “Unsteady aerodynamics of delta wings performing maneuvers to high angle of attack.” PhD diss., Stanford University.

Jonkman, J. M., B. J. Hayman, B. J. Jonkman, R. Damiani, and R. E. Murray. 2015. “AeroDyn v15 user’s guide and theory manual.” *NREL Draft Report,* 46.

Jouannet, C., and P. Krus. 2002. “Lift coefficient predictions for delta wing under pitching motions.” In *32nd AIAA Fluid Dynamics Conference and Exhibit,* 2969.

———. 2007. “Modelling of high angle of attack aerodynamic.” In *25th AIAA Applied Aerodynamics Conference,* 4295.

Katz, J., and A. Plotkin. 2001. *Low-speed aerodynamics.* Vol. 13. Cambridge University Press.

Katz, J., and D. Weihs. 1979. “Large amplitude unsteady motion of a flexible slender propulsor.” *Journal of Fluid Mechanics* 90 (4): 713–723.

Kerhascoët, H., J. Laurent, A. Cerqueus, M. Sevaux, E. Senn, F. Hauville, and R. Coneau. 2016. “Methodology for optimal wind vane design.” In *OCEANS 2016-Shanghai,* 1–7. IEEE.

Kershner, R. B. 1971. “The law of sines and law of cosines for polygons.” *Mathematics Magazine* 44 (3): 150–153.

Krienes, K. 1941. *The elliptic wing based on the potential theory.* Technical report. NACA-TM-971.

Lamar, J. E. 1974. *Extension of leading-edge-suction analogy to wings with separated flow around the side edges at subsonic speeds.* Technical report. NASA-TR-R-428.

———. 1976a. “Prediction of vortex flow characteristics of wings at subsonic and supersonic speeds.” *Journal of Aircraft* 13 (7): 490–494.

———. 1976b. *Some recent applications of the suction analogy to vortex-lift estimates.* Technical report. NASA-TM-X-72785.

Lamar, J. E., and B. B. Gloss. 1975. *Subsonic aerodynamic characteristics of interacting lifting surfaces with separated flow around sharp edges predicted by a Vortex-Lattice Method.* Technical report. NASA-TN-D-7921.

Lan, C. E. 1982. “The unsteady suction analogy and applications.” *AIAA Journal* 20 (12): 1647–1656.

Larson, E. S. 1981. “Sharp-Edged Rectangular Wing Characteristics.” *Journal of Aircraft* 18 (10): 895–896.

———. 2012. “Crossflow drag of finite-length rectangular wing-bodies.” In *23rd Aerospace Sciences Meeting,* 451.

Lawrence, H. R. 1951. “The lift distribution on low aspect ratio wings at subsonic speeds.” *Journal of the Aeronautical Sciences* 18 (10): 683–695.

Lee, T., and L. S. Ko. 2016. “Experimental study of the vortex flow and aerodynamic characteristics of a reverse delta wing.” *Proceedings of the Institution of Mechanical Engineers, Part G: Journal of Aerospace Engineering* 230 (6): 1126–1138.

———. 2017. “Vortex flow and lift generation of a non-slender reverse delta wing.” *Proceedings of the Institution of Mechanical Engineers, Part G: Journal of Aerospace Engineering* 231 (13): 2438–2451.

LeMay, S. P., S. M. Batill, and R. C. Nelson. 1990. “Vortex dynamics on a pitching delta wing.” *Journal of Aircraft* 27 (2): 131–138.

Levin, D., and A. Seginer. 1982. “Chordwise and compressibility corrections for arbitrary planform slender wings.” *AIAA Journal* 20 (8): 1025–1030.

Ljung, L. 1995. *System identification toolbox: User’s guide.* MathWorks Incorporated Natick, MA, USA.

Lomax, H., and L. Sluder. 1951. *Chordwise and compressibility corrections to slender-wing theory.* Vol. 1105. US Government Printing Office.

Lowry, J. G., and E. C. Polhamus. 1957. *A method for predicting lift increments due to flap deflection at low angles of attack in incompressible flow.* Technical report. NACA-TN-3911.

Lowson, M. V., and A. J. Riley. 1995. "Vortex breakdown control by delta wing geometry." *Journal of Aircraft* 32 (4): 832–838.

Luckring, J. M. 2016. "Selected scientific and technical contributions of Edward C. Polhamus." In *34th AIAA Applied Aerodynamics Conference,* 3565.

Mahgoub, A. O., and L. Cortelezzi. 2020. "Vortex flow and aerodynamic performance of a reverse delta wing." *AIAA Journal* 58 (2): 537–549.

Moreira, J. L. R., A. L. A. Mesquita, L. F. Araujo, M. A. B. Galhardo, J. R. P. Vaz, and J. T. Pinho. 2020. "Experimental investigation of drivetrain resistance applied to small wind turbines." *Renewable Energy* 153:324–333.

Na, J., Q. Chen, and X. Ren. 2018. *Adaptive Identification and Control of Uncertain Systems with Non-smooth Dynamics.* Academic Press.

Okamoto, M., and A. Azuma. 2011. "Aerodynamic characteristics at low Reynolds number for wings of various planforms." *AIAA Journal* 49 (6): 1135–1150.

Pedersen, C. B., and R. Żbikowski. 2006. "An indicial-Polhamus aerodynamic model of insect-like flapping wings in hover." *WIT Transactions on State-of-the-Art in Science and Engineering* 4.

Polhamus, E. C. 1966. *A concept of the vortex lift of sharp-edge delta wings based on a leading-edge-suction analogy.* Technical report. NASA TN D-3767.

Singh, K., A. Hemmati, and D. H. Wood. 2012. "The Aerodynamic Characterization of Generic Tail Fin Shapes." *Wind Engineering* 36 (5): 493–507.

SKF. 2023. *The SKF model for calculating the frictional moment.* https://www.skf.com/binaries/pub12/Images/0901d1968065e9e7-The-{SKF}-model-for-calculating-the-frictional-moment_tcm_12-299767.pdf. Last accessed on 2022-10-23.

Traub, L. W. 1997. "Prediction of vortex breakdown and longitudinal characteristics of swept slender planforms." *Journal of Aiircraft* 34 (3): 353–359.

———. 2003. "Extending slender wing theory to not so slender wings." *Journal of Aircraft* 40 (2): 399–402.

Vaz, J. R. P., D. H. Wood, D. Bhattacharjee, and E. F. Lins. 2018. "Drivetrain resistance and starting performance of a small wind turbine." *Renewable Energy* 117:509–519.

Wood, D. H. 2011. *Small wind turbines: analysis, design, and application.* London: Springer.

Wright, A. K. 2005. *Aspects of the aerodynamics and operation of a small horizontal axis wind turbine.* PhD thesis, University of Newcastle.

Wright, A. K., and D. H. Wood. 2007. "Yaw rate, rotor speed and gyroscopic loads on a small horizontal axis wind turbine." *Wind Engineering* 31 (3): 197–209.

Wu, T. Y. T. 1961. "Swimming of a waving plate." *Journal of Fluid Mechanics* 10 (3): 321–344.

Appendix A. MATLAB Code for System Identification of Tail Fin Response

System Identification using gray box modeling as described in Sections 10 and 13.2, estimates some parameters of the model by maximizing the fit of the theoretical response to the measurements. This Appendix provides the Matlab code for the SI in those sections. It is intended to be an example of using SI for tail fin response estimation with gray box techniques. The code assumes steady wind speed and optimizes some of the model coefficients of a delta fin in Eqn. (8.2). It was used for example to generate Figure 30(b).

Comments are highlighted in red. All the Matlab SI routines assume the input data is equi-spaced in time.

```
indata=load(filename,'-ascii% The first column is time, the second is the yaw angle
yin=indata(:,2); % The yaw angle
data = iddata(yin,[],Ts); % This step seems necessary to process an ascii data file
data.OutputName = 'Yaw Angle';
data.OutputUnit = 'deg';
data.Tstart = 0;
data.TimeUnit = 's';
% Data for USBT solution
U=5; % Wind speed (m/s)
Itail=0.055; % Total tail fin inertia (kg m^2)
rho=1.2; % Air density (kg/m^3)
b0=0.078; % Tail fin span (m)
fa=(0.25*pi*rho*b0*b0);
Idash= Itail/fa; % Reduced inertia
c0=0.27; % Tail fin chord (m)
xp=0.443; % Tail boom length (m)
Kp = 0.91; % Potential flow coefficient = pi*AR/2
Kv= pi; % Vortex lift coefficient
Cdc=1.3; % Drag coefficient at 90 deg.
kf = 0.001;ks=0.0011;kd=0.0012;n=0.47; % Friction coefficients
s1=0.3; s2=0.1;s3=0.1; a1=39; a2=60; a3=60; % Aerodynamic initial parameters
A1=c0*(0.2*c0*c0+ 0.5*xp*c0+xp*xp/3); % Added Inertia coefficient
A2=U*(c0+xp)*(c0+xp);% Aerodynamic damping coefficient of potential flow
A2_1=U*(0.5*c0^2+4/3*c0*xp+xp^2); % Aerodynamic damping coefficient of vortex flow
A2_2=2/5*c0^3+3/2*xp*c0^2+2*xp^2*c0+xp^3; % Damping coefficient of (d gamma/dt)^2
A3=U*U*(2*c0/3+xp); % Steady state term coefficient
g=-40*pi/180; % Initial yaw angle
g0=0; % Initial yaw rate
nonlinear_model = idnlgrey('NLinearYaw_m2',[1 0 5],[fa;Idash; A1; A2;A2_1;A2_2; A3; ...
Kp; Kv; Cdc; s1; s2;s3; a1; a2;a3; kf; ks; kd; n],[g; g0; x10; x20; x30],0); setpar(nonlinear_model,'Fixed', true true
true true true true true true true true ...
true true true true true true true true true false )
% Use the nonlinear gray box SI Matlab routine and set the free parameters
% Specify range of the free parameters:
nonlinear_model.Parameters(11).Minimum=0;nonlinear_model.Parameters(11).Maximum=2; % Range of sigma_1
nonlinear_model.Parameters(12).Minimum=0;nonlinear_model.Parameters(12).Maximum=2; % Range of sigma_2
nonlinear_model.Parameters(13).Minimum=0;nonlinear_model.Parameters(13).Maximum=2; % Range of sigma_3
nonlinear_model.Parameters(14).Minimum=30;nonlinear_model.Parameters(14).Maximum=40; % Range of al-
pha*_1
nonlinear_model.Parameters(15).Minimum=40;nonlinear_model.Parameters(15).Maximum=60; % Range of al-
pha*_2
nonlinear_model.Parameters(16).Minimum=60;nonlinear_model.Parameters(16).Maximum=80; % Range of al-
pha*_3
nonlinear_model.Parameters(20).Minimum= 0;nonlinear_model.Parameters(20).Maximum=1; % Range of n_s
nlgreyest(data,nonlinear_model,'Display','Full',opt);
```

```
getpvec(nonlinear_model,'free')
figure;
compare(data,nonlinear_model) %This command produces figures like 30(b)
xlabel('Time,s')
ylabel('Yaw angle, gamma')
end
% The function NLinearYaw_m2 :
function [dx,y] = NLinearYaw_m2(t, x, u, fa, Idash, A1, A2, A2_1,A2_2, A3, Kp, Kv, Cdc,...
s1, s2, s3, a1, a2, a3, kf, ks, kd, n, varargin)
% Calculate x_i values
x1=1/(1+exp(s1*(180/pi*abs(x(1))-a1)));
x2=1/(1+exp(s2*(180/pi*abs(x(1))-a2)));
x3=1/(1+exp(s3*(180/pi*abs(x(1))-a3)));
% Output equation:
y=x(1)*180/pi;
% The state equations:
dx=[x(2); -((A2*x1*cos(x(1))+2*A2_1*x2*Kv/Kp*abs(sin(x(1)))+2*A2_1*(1-...
x3)*Cdc/Kp*abs(sin(x(1))))*x(2) +A2_2*(x2*Kv/Kp*abs(x(2))+...
(1-x3)*Cdc/Kp*abs(x(2)))*x(2)+A3(x1*cos(x(1))*sin(x(1))+...
x2*Kv/Kp*sin(x(1))*abs(sin(x(1)))+(1-x3)*Cdc/Kp*sin(x(1))))/(Idash+A1)-...
(kf*abs(x(2))^0.6*sign(x(2))+ks*sign(x(2))+(kd)*exp(-(x(2)/n)^2)*...
sign(x(2)))/(Idash+A1)/fa;
end
```

Part of the input data file is :

```
0 -41.7
0.001 -41.55
0.002 -41.55
0.003 -41.55
0.004 -41.55
0.005 -41.55
0.006 -41.55
0.007 -41.55
0.008 -41.55
0.009 -41.55
0.01 -41.55
0.011 -41.55
0.012 -41.55
0.013 -41.55
0.014 -41.55
0.015 -41.55
0.016 -41.55
0.017 -41.55
0.018 -41.55
0.019 -41.55
0.02 -41.55
0.021 -41.55
0.022 -41.55
0.023 -41.55
0.024 -41.55
0.025 -41.55
0.026 -41.55
0.027 -41.55
0.028 -41.55
```

0.029 -41.55
0.03 -41.55
0.031 -41.55
0.032 -41.4
.....
4.424 0.45
4.425 0.45
4.426 0.45
4.427 0.45
4.428 0.45
4.429 0.45
4.43 0.45
4.431 0.45
4.432 0.6
.....
8.805 1.2
8.806 1.35
8.807 1.35
8.808 1.35
8.809 1.35

where the first column is the measured time in seconds and the second is the yaw angle in deg. The code needs only the second column while the sampling time $T_s = 0.001s$ for this case is input. The last lines of data show the tail fin stopping angle $\gamma_s = 1.35^\circ$, see Eqn. (9.1).